

Anisotropic Gent–McWilliams Parameterization for Ocean Models

RICHARD D. SMITH

Theoretical Division, Los Alamos National Laboratory, Los Alamos, New Mexico

PETER R. GENT

National Center for Atmospheric Research, Boulder, Colorado*

(Manuscript received 20 October 2003, in final form 5 April 2004)

ABSTRACT

An anisotropic generalization of the Gent–McWilliams (GM) parameterization is presented for eddy-induced tracer transport and diffusion in ocean models, and it is implemented in an ocean general circulation model using a functional formalism to derive the spatial discretization. This complements the anisotropic viscosity parameterization recently developed by Smith and McWilliams. The anisotropic GM operator is potentially useful in both coarse- and high-resolution ocean models, and in this study the focus is on its application in high-resolution eddying solutions, for which it provides an adiabatic alternative to the more commonly used biharmonic horizontal diffusion operators. It is shown that realistically high levels of eddy energy can be simulated using harmonic anisotropic diffusion and friction operators. Isotropic forms can also be used, but these tend either to overly damp the solution when a large diffusion coefficient is used or to introduce unacceptable levels of numerical noise when a small coefficient is used. A series of numerical simulations of the North Atlantic Ocean are conducted at 0.2° resolution using anisotropic viscosity, anisotropic GM, and biharmonic mixing operators to investigate the effects of the anisotropic forms and to isolate changes in the solutions specifically associated with anisotropic GM. A high-resolution 0.1° simulation is then conducted using both anisotropic forms, and the results are compared with a similar run using biharmonic mixing. Modest improvements are seen in the mean wind-driven circulation with the anisotropic forms, but the largest effects are due to the anisotropic GM parameterization, which eliminates the spurious diapycnal diffusion inherent in horizontal tracer diffusion. This leads to significant improvements in the model thermohaline circulation, including the meridional heat transport, meridional overturning circulation, and deep-water formation and convection in the Labrador Sea.

1. Introduction

Traditionally, numerical models of ocean circulation with a horizontal resolution of 0.5° and finer have used biharmonic diffusion operators for viscosity and diffusivity, starting with the work of Semtner and Mintz (1977). The main reason is that the biharmonic forms are much more scale selective; they more effectively eliminate noise generated by numerical truncation error on the grid scale, but introduce less damping of the larger scales, thereby allowing higher levels of eddy kinetic energy and tracer variance. However, in z -coordinate models, horizontal diffusion, whether harmonic or biharmonic, produces spurious diapycnal mixing of tracers across sloping isopycnals that is much larger than the observed diapycnal mixing in the ocean. In addition,

it has recently been shown that biharmonic diffusion produces sign-indefinite tracer fluxes that can lead to unphysical cabelling (Griffies 2004, section 14.5).

In non-eddy-resolving models, which we define as a horizontal resolution of 1° or coarser, large improvements have been found by aligning the harmonic diffusion of tracers along isopycnal surfaces and by introducing an extra eddy-induced advection term that acts to flatten isopycnal slopes. This is the Gent–McWilliams (GM) parameterization (see Gent and McWilliams 1990, hereinafter GM90). These improvements include a more realistic density structure, stronger meridional overturning and poleward heat transport, and a much better representation of eddy effects on the Antarctic Circumpolar Current and the localized regions of deep water formation. There has been some confusion in the literature as to what is meant by the GM parameterization. Sometimes it is regarded as just an advective parameterization, but we define it to be the sum of the eddy-induced transport plus the diffusion of tracers along isopycnal surfaces. The eddy-induced transport can be thought of as arising from the correlations between perturbations of velocity and isopycnal layer thickness. The GM form

* The National Center for Atmospheric Research is sponsored by the National Science Foundation.

Corresponding author address: Peter R. Gent, National Center for Atmospheric Research, P.O. Box 3000, Boulder, CO 80307-3000.
E-mail: gent@ucar.edu

of the eddy-induced advection mimics the effect of releasing the potential energy stored in sloping isopycnals through baroclinic instability.

All downgradient diffusive parameterizations are ultimately derived from stochastic random-walk models of turbulent fluid transport. Dukowicz and Smith (1997) showed that the GM parameterization can be derived from the simplest version of a stochastic random-walk model applied to turbulent fluid motion within an isopycnal layer, which obeys the same transport equation as a 2D compressible fluid. Furthermore, this theory predicts that both the eddy-induced transport and diffusion terms are specified by the same along-isopycnal diffusion tensor. In general, this tensor may be either isotropic or anisotropic depending on the nature of the underlying turbulence. It may vary in both space and time, and should be large in regions of strong turbulence and small in regions of weak turbulence.

Most applications of GM have used a single globally constant diffusion coefficient for both transport and diffusion terms, which is set by its appropriate value in strong currents. Visbeck et al. (1997) proposed a spatially and temporally variable coefficient based on the local Eady time scale for growth of unstable baroclinic disturbances. This has been used in place of a constant coefficient to try to account for the variability of the strength of turbulent mixing. When the GM scheme has been used in the eddy regime with a constant coefficient, the solutions are either less energetic or very noisy in comparison with results using biharmonic closures, depending on whether a large or small GM coefficient is used. In a suite of 0.4° North Atlantic experiments (F. O. Bryan 2003, personal communication) it was found that using a large constant and isotropic GM coefficient maximizes the northward heat transport but damps nearly all of the eddy energy, and the solution looks similar to a non-eddy-resolving solution in a 1° model. As shown in the 0.2° simulations presented here, solutions using isotropic GM with a small coefficient allow more eddy activity but tend to exhibit excessive numerical noise.

Roberts and Marshall (1998) proposed a biharmonic form of the GM eddy-induced advection term and showed that the improvements continued well into the eddy regime, down to $1/8^\circ$. They used a model with only one active tracer, temperature, so that isotherms coincided with isopycnals and therefore tracer diffusion along isopycnals was not required. A biharmonic along-isopycnal diffusion operator is frequently used in isopycnal coordinate models but has not been implemented in z -coordinate models. In principle this could be done, but it would be difficult because there are fourth-order vertical derivatives that have to be solved implicitly if the isopycnal slopes are larger than the gridcell aspect ratio. Furthermore, it is possible that other terms involving mixed horizontal and vertical derivatives would also have to be treated implicitly, and this would require the solution of a global implicit system. For these rea-

sons, biharmonic isopycnal diffusion operators have not been successfully developed and implemented in z -coordinate models. To date there are no published eddy solutions in z -coordinate models with horizontal resolution of 0.1° or higher that employ adiabatic diffusion schemes.

Solutions using 0.1° resolution are commonly called eddy resolving, but it is not clear that this is entirely correct. Solutions with higher resolution must be performed to test the convergence properties of these solutions. In fact, one definition of eddy resolving might be the resolution at which the solutions are almost independent of the eddy parameterization. The work in this paper and the companion paper of Bryan et al. (2004, unpublished manuscript, hereinafter BHS) shows that North Atlantic Ocean solutions at 0.1° still depend on the eddy parameterization used.

In non-eddy-resolving models, improvements to the ocean currents can be obtained by using an anisotropic form of the horizontal viscosity. Large et al. (2001) show that this form gives much stronger, narrower, and more realistic equatorial and boundary currents. Smith and McWilliams (2003, hereinafter SM2003) give a general formulation that allows the anisotropy to be in any chosen direction, but they only show numerical solutions from a simple zonal channel geometry. In this work, this general form is implemented in realistic 0.2° - and 0.1° -resolution runs for a North Atlantic Ocean domain. It is shown that anisotropic harmonic viscosity, with the appropriate choice of coefficients, can produce levels of mean and eddy kinetic energy that are as large as using biharmonic viscosity, and without introducing excessive noise into the solution.

The original justification for anisotropic viscosity was to get around the Munk and grid Reynolds number constraints in non-eddy-resolving models, so that small cross-stream viscosity coefficients could be used in the ocean interior. SM2003 discuss further justifications for anisotropic viscosity. Analyses of laboratory experimental data suggest that momentum and tracer diffusion occurs preferentially along the axis of a turbulent jet, and is weaker across the jet. In addition, a number of numerical studies have shown that tracer dispersion by mesoscale eddies occurs more strongly in the zonal than in the meridional direction because of the beta effect; see Holloway and Kristmannsson (1984), Haidvogel and Keffer (1984), Bartello and Holloway (1991), and Figueroa and Olson (1994). As discussed by SM2003, a similar topographic beta effect may lead to stronger turbulent dispersion along compared to across contours of constant f/H , where f is the Coriolis frequency and H is the ocean depth. Thus, there is a little, but not much, justification for using an anisotropic form of the GM parameterization. At the resolutions used in this study, what is being parameterized is the effect of 10-km and smaller eddies and turbulence on the resolved mean flow and eddies of resolution 20 km and larger. As far as we are aware, this effect has not been diagnosed either from numerical models that use a horizontal resolution of 1

km or finer, or directly from ocean observations. However, observations do show that diapycnal diffusivity is very small in many locations below the mixed layer away from boundaries. This very strongly suggests that the effects of 10-km-scale eddies and turbulence on the larger scale flows must be adiabatic.

The anisotropic GM parameterization proposed in this work is a natural extension of the anisotropic viscosity formulation developed in SM2003. The anisotropy is determined by a field of unit vectors that specify a preferred direction at each point in space, which breaks the transverse isotropy, and by two coefficients for tracer diffusion parallel and perpendicular to this direction. In addition, anisotropic GM allows more flexibility in handling numerical constraints. As discussed in Large et al. (2001) and SM2003, the two numerical constraints on the minimum allowed viscosity can be separately satisfied by the along- and cross-stream viscous coefficients. These are the Munk constraint, required to resolve western boundary currents, and the grid Reynolds number constraint, required to damp noise generated by the nonlinear momentum advection term. In the case of diffusion, there is no analog to the Munk constraint, but the coefficient must still be large enough to diffuse noise generated on the grid scale by the nonlinear tracer advection term. As with the anisotropic viscosity, experience has shown that this can be accomplished using anisotropic GM with a sufficiently large along-stream diffusivity, while the cross-stream diffusivity may be chosen as small as desired. In fact, in simulations with anisotropic GM presented in this paper, we chose to have the extreme value of 0 cross-stream diffusivity.

The GM parameterization was originally derived to apply to the adiabatic interior ocean, and the issue of how to extend it to the boundaries or boundary layers was not addressed. In most applications, the GM parameterization is turned off immediately adjacent to boundaries and in the diabatic mixed layer at the ocean surface. If the GM scheme, with usual values of the coefficient, is applied in the mixed layer, then the GM tendency to flatten isopycnals overcomes the vertical mixing that keeps the isopycnals very steep or vertical. There is strong diapycnal mixing in the mixed layer, which can be approximated as horizontal diffusion; see Treguier et al. (1997). We will investigate the use of horizontal diffusion replacing GM in the mixed layer in some of the simulations presented in this paper.

The paper is organized as follows: In section 2 the mathematical formulation of the anisotropic GM parameterization is presented. Section 3 briefly describes the setup of the 0.2° and 0.1° North Atlantic Ocean domains, the parameterizations used, and the atmospheric observations used for the surface wind stress and buoyancy forcing. Section 4 describes results from integrations of the 0.2° configuration that use various viscosity and diffusion parameterizations. Results from the 0.1° North Atlantic simulations are presented in section 5, two with anisotropic and one with biharmonic parameterizations

both of viscosity and diffusivity. Section 6 is a discussion of the main results and conclusions. In the appendix, a functional discretization of the anisotropic GM operator is presented that ensures positive-definite diffusion of tracer variance. The boundary conditions on the operator are discussed, and it is shown that in the anisotropic case it is not necessary to set the diffusivity to 0 immediately adjacent to the boundaries.

2. Mathematical formulation of anisotropic GM

In the GM closure scheme the continuity and tracer transport equations are given in isopycnal coordinates $(\tilde{x}, \tilde{y}, \rho, \tilde{t})$, where \tilde{x} and \tilde{y} are horizontal general orthogonal coordinates on the surface of the sphere, by

$$\partial_{\tilde{t}} h + \tilde{\nabla} \cdot h(\mathbf{u} + \mathbf{u}^*) = 0 \quad \text{and} \quad (1)$$

$$\partial_{\tilde{t}} \phi + (\mathbf{u} + \mathbf{u}^*) \cdot \tilde{\nabla} \phi = \frac{1}{h} \tilde{\nabla} \cdot h \mathbf{K} \cdot \tilde{\nabla} \phi, \quad (2)$$

where ϕ is the tracer field, $h = -\rho_o \partial_{\rho} z$ is the isopycnal layer thickness, and \mathbf{u} is horizontal velocity; $\tilde{\nabla} = (\partial_{\tilde{x}}, \partial_{\tilde{y}})$, and the partial derivatives $\partial_{\tilde{t}}$, $\partial_{\tilde{x}}$, and $\partial_{\tilde{y}}$ are understood to act along constant density surfaces. Here \mathbf{K} is a 2×2 along-isopycnal symmetric mixing tensor for tracer diffusion, which has the general form

$$\mathbf{K} = \begin{pmatrix} K_{xx} & K_{xy} \\ K_{xy} & K_{yy} \end{pmatrix}, \quad (3)$$

where the subscripts x and y denote the two horizontal directions.

There have been a number of proposals for the form of the eddy-induced velocity. GM90 originally proposed

$$\mathbf{u}^* = \frac{\rho_o}{h} \partial_{\rho} (\mathbf{K}' \cdot \mathbf{L}), \quad (4)$$

where $\mathbf{L} = \tilde{\nabla} z$ is the isopycnal slope vector, and \mathbf{K}' is another 2×2 tensor for the eddy-induced velocity. In applications it is commonly assumed that $\mathbf{K}' = \mathbf{K}$. The stochastic theory of adiabatic stratified turbulence (Dukowicz and Smith 1997; Smith 1999) predicts $\mathbf{K}' = \mathbf{K}$, but the eddy-induced velocity has a slightly different form given by

$$\mathbf{u}^* = -\frac{1}{h} \mathbf{K}' \cdot \tilde{\nabla} h. \quad (5)$$

Note that (4) and (5) are equivalent if \mathbf{K}' is independent of density (or depth). The stochastic theory was developed by considering turbulent flow within a single isopycnal layer where the diffusivity tensor depends only on x and y , and so in fact it cannot distinguish between these two forms. For a number of reasons, we prefer to use the GM90 form (4). First, it has the great advantage that it is very easy to impose boundary conditions at the ocean surface and bottom so that the eddy-induced velocity does not contribute to the barotropic mode. Killworth (1997) shows this is a necessary criterion so

that the eddy parameterization is not a source of momentum if the eddy term is put into the momentum equation. Second, McDougall and McIntosh (2001, their section 11) argue that uncertainty in the boundary conditions for the form (5) can lead to a false overturning circulation and incorrect poleward heat transport due to the eddies. Last, while it can be shown that both forms lead to a reduction in available potential energy by flattening isopycnals, Gent et al. (1995) show that, in the energy budget equations, the form (4) leads to a local negative-definite sink of mean potential energy. We think this is advantageous both physically and numerically.

The tracer transport and continuity equations in level coordinates (x, y, z, t) are given by

$$\nabla_3 \cdot \mathbf{u}_3 = \nabla_3 \cdot \mathbf{u}_3^* = 0, \quad (6)$$

$$\partial_t \phi + (\mathbf{u}_3 + \mathbf{u}_3^*) \cdot \nabla_3 \phi = \nabla_3 \cdot \mathbf{K}_3 \cdot \nabla_3 \phi \equiv \mathcal{D}(\phi), \quad (7)$$

$$\mathbf{u}^* = -\partial_z(\mathbf{K}' \cdot \mathbf{L}), \quad \text{and} \quad (8)$$

$$w^* = \nabla \cdot (\mathbf{K}' \cdot \mathbf{L}). \quad (9)$$

The slope vector in level coordinates is given by $\mathbf{L} = -\rho_z^{-1} \nabla \rho$, where $\nabla = (\partial_x, \partial_y)$ is the horizontal gradient at constant z . The subscript 3 indicates three-dimensional vectors or a 3×3 tensor. Thus $\nabla_3 = (\nabla, \partial_z)$, and $\mathbf{u}_3 = (\mathbf{u}, w)$, where \mathbf{u} and w are the horizontal and vertical velocities. Similarly $\mathbf{u}_3^* = (\mathbf{u}^*, w^*)$. This simple analytic form of w^* results from using the GM90 form (4) for \mathbf{u}^* . For the transformation of the transport equations from isopycnal to level coordinates, see, for example, Smith (1999, his appendix B). The second-order diffusion tensor \mathbf{K}_3 is given by

$$\mathbf{K}_3 = \begin{pmatrix} \mathbf{K} & \mathbf{K} \cdot \mathbf{L} \\ \mathbf{K} \cdot \mathbf{L} & \mathbf{L} \cdot \mathbf{K} \cdot \mathbf{L} \end{pmatrix}. \quad (10)$$

Here \mathbf{K}_3 appears to be a 2×2 tensor, but is actually 3×3 since \mathbf{K} is a 2×2 tensor. In the isotropic limit, \mathbf{K} is proportional to the 2×2 unit tensor: $\rightarrow \kappa \mathbf{1}$, and the above equations reduce to the standard isotropic GM formulation, and \mathbf{K}_3 reduces to the small-slope version of the Redi diffusion tensor [Eq. (13) of Gent et al. 1995].

With a nonlinear equation of state, the isopycnal slope $\mathbf{L} = (L_x, L_y)$ should be replaced by the slope along the local neutral surface (McDougall 1987), which is given by

$$L_x = -\frac{\alpha_p \Theta_x - \beta_p S_x}{\alpha_p \Theta_z - \beta_p S_z}, \quad (11)$$

with a similar definition for L_y . Here $\alpha_p = -\partial \rho_p / \partial \Theta$ and $\beta_p = \partial \rho_p / \partial S$, where Θ and S are the model potential temperature and salinity, and ρ_p is the potential density referenced to the local pressure (or depth). Subscripts on the tracer fields denote partial derivatives: $\Theta_x = \partial_x \Theta$, and so on. We will continue to refer to $\mathcal{D}(\phi)$ in (7) as the ‘‘isopycnal’’ diffusion operator, but in general the tensor \mathbf{K} should be understood to diffuse along neutral, rather than isopycnal, surfaces.

a. Specification of \mathbf{K}

Our intent is to construct an anisotropic form of the 2×2 isopycnal diffusion tensor \mathbf{K} , which is symmetric and positive-definite. The most general form can be constructed from an arbitrary symmetric anisotropic 2D tensor s_{ij} and the symmetric isotropic tensor δ_{ij} , where δ_{ij} , the 2D Kronecker delta, is the only symmetric and isotropic rank-2 tensor:

$$K_{ij} = a\delta_{ij} + bs_{ij}. \quad (12)$$

Following SM2003, we wish to find an anisotropic form of \mathbf{K} , which is associated with a given direction that breaks the transverse isotropy. To accomplish this, consider a field of horizontal unit vectors $\hat{\mathbf{n}}$ defined at each point in space. The only symmetric rank-2 anisotropic tensor that can be constructed from $\hat{\mathbf{n}}$ alone is the 2×2 dyadic tensor

$$s_{ij} = n_i n_j, \quad \hat{\mathbf{n}} = (n_x, n_y), \quad \text{and} \quad n_x^2 + n_y^2 = 1. \quad (13)$$

This completes the specification of \mathbf{K} in terms of $\hat{\mathbf{n}}$, except that the coefficients a and b must be chosen such that \mathbf{K} is positive-definite, or equivalently, such that the eigenvalues of \mathbf{K} are nonnegative. The two eigenvalues of \mathbf{K} are given by $A = a + b$ and $B = a$. In terms of these, \mathbf{K} takes the form

$$\mathbf{K} = \begin{pmatrix} An_x^2 + Bn_y^2 & (A - B)n_x n_y \\ (A - B)n_x n_y & Bn_x^2 + An_y^2 \end{pmatrix} \quad (14)$$

and \mathbf{K} is positive-definite provided $A \geq 0$ and $B \geq 0$. Note that \mathbf{K} is invariant under $\hat{\mathbf{n}} \rightarrow -\hat{\mathbf{n}}$. The standard isotropic form is recovered in the limit $A = B$, where \mathbf{K} becomes proportional to the 2×2 unit tensor. In general, A is the coefficient for diffusion along the direction $\hat{\mathbf{n}}$, and B is the coefficient for diffusion perpendicular to the direction $\hat{\mathbf{n}}$. To show this, we note that K_{ij} in (12) is invariant and may be evaluated in any coordinate system. If we rotate the coordinates so that locally $\hat{\mathbf{n}}$ is oriented along the x coordinate ($n_x = 1, n_y = 0$), and choose $B = 0$, then the only non-0 element of \mathbf{K} is K_{xx} , and the mixing is one-dimensional along the direction $\hat{\mathbf{n}}$ with coefficient A . Alternatively, if we choose $A = 0$, then only K_{yy} is nonzero, and the mixing is one-dimensional along the y coordinate, normal to $\hat{\mathbf{n}}$, with coefficient B .

b. Skew-flux form of the eddy-induced transport

The eddy-induced tracer transport term in (7) can be written such that it has the form of a diffusion operator with an antisymmetric mixing tensor: where

$$-\mathbf{u}_3^* \cdot \nabla_3 \phi = \nabla_3 \cdot \mathbf{A}_3 \cdot \nabla_3 \phi \equiv \mathcal{B}(\phi), \quad (15)$$

where

$$\mathbf{A}_3 = \begin{pmatrix} 0 & -\mathbf{K}' \cdot \mathbf{L} \\ \mathbf{K}' \cdot \mathbf{L} & 0 \end{pmatrix}. \quad (16)$$

This simple analytic form of \mathbf{A}_3 again results from using

TABLE 1. List of 0.2° and 0.1° North Atlantic simulations: biharmonic viscosities and diffusivities ($\text{m}^4 \text{s}^{-1}$) and along-stream (A) and cross-stream (B) anisotropic viscosities and diffusivities ($\text{m}^2 \text{s}^{-1}$). Runs AII', AA2', and A' all include horizontal harmonic diffusion in the upper ocean where the GM diffusivities are normally tapered (see section c of the appendix).

Run	Resolution	Integration period	Viscosity	Diffusivity
BB	$0.2^\circ \times 0.2^\circ \cos\phi$	Feb 1986–Jan 1997	Biharmonic, $-21.6 \times 10^{10} \cos^3\phi$	Biharmonic, $-7.2 \times 10^{10} \cos^3\phi$
AB	''	''	Anisotropic, $A = 300, B = 30$	''
AA1	''	''	''	Anisotropic GM, $A = 50, B = 0$
AII	''	''	''	Isotropic GM, $A = 50, B = 50$
AA2	''	''	''	Anisotropic GM, $A = 500, B = 0$
AII2	''	''	''	Isotropic GM, $A = 500, B = 500$
AII'	''	Nov 1990–Jan 1997	''	Isotropic GM + horizontal diffusion, $A = B = 50$
AA2'	''	''	''	Anisotropic GM + horizontal diffusion, $A = 500, B = 0$
B	$0.1^\circ \times 0.1^\circ \cos\phi$	Jan 1986–Mar 2001	Biharmonic, $-1.35 \times 10^{10} \cos^3\phi$	Biharmonic $-0.45 \times 10^{10} \cos^3\phi$
A	''	''	Anisotropic, $A = 150 \cos\phi, B = 5 \cos\phi$	Anisotropic GM, $A = 150 \cos\phi, B = 0$
A'	''	Feb 1996–Mar 2001	''	Anisotropic GM + horizontal diffusion, $A = 150 \cos\phi, B = 0$

the GM90 form (4) of \mathbf{u}^* . As in (10) this appears to be a 2×2 tensor but is actually a 3×3 tensor. The eddy induced transport in this form is the divergence of the so-called skew flux, $-\mathbf{A}_3 \cdot \nabla_3 \phi$. Using (16), the tracer transport equation takes the form

$$\partial_t \phi + \mathbf{u}_3 \cdot \nabla_3 \phi = \nabla_3 \cdot (\mathbf{K}_3 + \mathbf{A}_3) \cdot \nabla_3 \phi. \quad (17)$$

As pointed out by Griffies (1998), with the assumption $\mathbf{K}' = \mathbf{K}$ the combined tensor on the right-hand side of (17) takes the simpler form

$$\mathbf{K}_3 + \mathbf{A}_3 = \begin{pmatrix} \mathbf{K} & 0 \\ 2\mathbf{K} \cdot \mathbf{L} & \mathbf{L} \cdot \mathbf{K} \cdot \mathbf{L} \end{pmatrix}. \quad (18)$$

In the simulations presented in this paper we assume $\mathbf{K}' = \mathbf{K}$ and use the simple form (18) in the numerical discretization of the GM transport and diffusion operators [see the appendix, Eq. (A3)].

3. Model configurations

We now investigate the use of both anisotropic GM and the anisotropic viscosity in comparison with biharmonic forms in a series of eddy simulations of the North Atlantic Ocean. The solutions have 0.2° and 0.1° horizontal resolution and use the Los Alamos Parallel Ocean Program (POP); see Smith et al. (1992) and Smith and Gent (2002). These runs are configured very similarly to the 0.1° North Atlantic simulation described in Smith et al. (2000, hereinafter SMBH). Most of the simulations were conducted at the less expensive 0.2° resolution to sort out the effects of the different mixing parameterizations before conducting the more expensive 0.1° runs. A list of all the 0.2° and 0.1° experiments is given in Table 1, and they all used the second-order, centered advection scheme.

Section 2 of SMBH describes the North Atlantic model configuration in considerable detail, so that only a brief overview will be given here. The model domain extends from 20°S to 72.6°N and from 98°W to 17.2°E and excludes the eastern part of the Mediterranean Sea and Hudson Bay. There are buffer zones near the northern and southern boundaries and in the western Mediterranean Sea, where the potential temperature and salinity are restored to the seasonal Levitus (1982) values at all depths, with a restoring time scale that varies linearly from 15 to 0 days across the 3° -wide buffer zones. A Mercator grid is used in the horizontal direction with a zonal resolution of $\Delta\lambda = 0.2^\circ$ and 0.1° in the two configurations, where λ is longitude. The meridional resolution is $\Delta\phi = 0.2^\circ$ (0.1°) $\cos\phi$, where ϕ is latitude. The vertical grid has 40 nonuniform levels that vary smoothly in thickness from 10 m at the surface to 250 m at depth, and realistic topography is interpolated to the grids.

The wind stress was derived from the European Centre for Medium-Range Weather Forecasts (ECMWF) Tropical Ocean and Global Atmosphere (TOGA) analysis covering the model integration periods of 1986–96 for the 0.2° runs and 1986–February 2001 for the 0.1° runs. Daily values of stress were calculated from the 10-m winds and interpolated to the model grids. The surface heat flux was derived from the seasonal climatology of Barnier et al. (1995), except that the solar radiation was allowed to penetrate in depth. The equivalent salt flux was simulated by restoring the surface salinity to the monthly Levitus (1982) climatology with a 1-month restoring time scale over the upper level depth of 10 m. The models were initialized to January Levitus (1982) climatology and a state of rest. This produces initial transients, and a 0.2° run with isotropic mixing

and a small time step was performed for 1 month to overcome the initial transients. The 0.2° runs were started, using a larger time step, from the end of this short run at the beginning of February 1986.

a. 0.2° configuration and experiments

In this configuration, vertical viscosities and diffusivities were computed, using the Pacanowski and Philander (1981) Richardson number formulation, with background values of 10^{-4} and $10^{-5} \text{ m}^2 \text{ s}^{-1}$, respectively. As required by the GM parameterization, the vertical mixing terms were solved implicitly (see the appendix). SMBH used explicit vertical mixing combined with two passes through a convective adjustment scheme, but for consistency all runs presented in this paper use implicit vertical mixing without convective adjustment. A quadratic bottom stress was used, with a drag coefficient of 1.225×10^{-3} . The parameters for viscosity and diffusivity used in these experiments are given in Table 1. The first experiment, BB, used horizontal biharmonic viscosity and diffusivity. The coefficients vary spatially with the cube of the horizontal grid spacing and have equatorial values of -2.16×10^{11} and $-7.2 \times 10^{10} \text{ m}^4 \text{ s}^{-1}$, respectively. The second experiment, AB, had the same biharmonic diffusion but used the anisotropic viscosity described in SM2003, with the anisotropy aligned with the instantaneous flow direction: $\hat{\mathbf{n}} = \mathbf{u}/|\mathbf{u}|$. The along-stream viscosity of $300 \text{ m}^2 \text{ s}^{-1}$ was an order of magnitude larger than the cross-stream viscosity of $30 \text{ m}^2 \text{ s}^{-1}$. The cross-stream viscosity was chosen as the minimal value at this resolution that satisfies the Munk constraint [see SM2003, their (37)]. A preliminary set of 0.2° experiments had shown that anisotropic viscosity can give KE levels comparable to those using biharmonic viscosity, and the coefficients used in the AB experiment were designed to give KE levels comparable to those of the BB experiment. It was then decided to use the anisotropic viscosity formulation for the remaining experiments that explore the anisotropic GM formulation. This was for consistency with the single 0.1° anisotropic run, which uses both anisotropic forms.

Four experiments were run with different choices of the GM coefficients. The third and fourth experiments in Table 1, AA1 and AI1, use anisotropic and isotropic GM, respectively, and a small coefficient of $50 \text{ m}^2 \text{ s}^{-1}$ for the along-stream and isotropic diffusivities. The fifth and sixth experiments, AA2 and AI2, are similar except they use a large value of $500 \text{ m}^2 \text{ s}^{-1}$ for the along-stream and isotropic diffusivities. In all of the anisotropic GM runs, $\hat{\mathbf{n}}$ is aligned with the local flow direction, and we chose to use the extreme value of 0 for the cross-stream diffusivity. As discussed in the introduction, it is only necessary that the along-stream diffusivity be nonzero to control numerical noise generated by the advection operator.

There is one more difference between the biharmonic

diffusion and GM experiments. The biharmonic diffusion acts everywhere, and the coefficient is never tapered. In contrast, tapering of the GM diffusion tensor is applied following the scheme described in appendix B of Large et al. (1997). The first taper function is applied when the isopycnal slope is steep, because of numerical stability requirements. However, the maximum slope is now set to 0.3 rather than the lower value of 0.01 used by Large et al. The much larger maximum slope now used means that this tapering does not apply very often. Large et al. also found that a second tapering was necessary near the ocean surface to prevent the GM scheme from overwhelming the vertical mixing in the upper boundary layer. This tapering turns off the GM scheme in the upper ocean, so that there is no isopycnal tracer diffusion there at all. We found that this leads to numerical noise in the upper ocean in the runs with GM. As noted in the introduction, Treguier et al. (1997) propose that there should be horizontal tracer mixing in the boundary layer, where the isopycnal slopes are very steep. Implementing horizontal diffusion to replace the GM scheme where it is tapered is very easy if the coefficients are assumed to be equal. The method for doing this is described in section c of the appendix. It can be thought of as simply rotating the diffusion operator, whether isotropic or anisotropic, to be horizontal rather than isopycnal within the mixed layer. Two 5-yr runs with this modification have been made, called AI1' and AA2', which are branch runs beginning in November 1990 from AI1 and AA2, respectively. In these runs the numerical noise in the upper ocean seen in AI1 and AA2 is substantially reduced, which will be documented more fully below.

b. 0.1° configuration and experiments

A different vertical mixing scheme was used in the two 0.1° experiments. It is the *K*-profile parameterization (KPP) scheme of Large et al. (1994), which is now used in several ocean components of climate models. Note that this scheme is not used in the 0.1° simulation described in SMBH.

Because of the higher computational cost of the 0.1° model, only two experiments have been run. The first experiment, B in Table 1, used both biharmonic viscosity and diffusion with coefficients of -1.35×10^{10} and $-0.45 \times 10^{10} \text{ m}^4 \text{ s}^{-1}$, respectively. Again, the coefficients vary spatially with the cube of the horizontal grid spacing to compensate for the merging meridians at high latitudes. The second experiment, A, uses both anisotropic viscosity and GM. The along-stream viscosity coefficient is $150 \cos\phi \text{ m}^2 \text{ s}^{-1}$, and the cross-stream coefficient is much smaller at $5 \cos\phi \text{ m}^2 \text{ s}^{-1}$. This is again the smallest value that satisfies the Munk constraint. The along-stream GM coefficient is also $150 \cos\phi \text{ m}^2 \text{ s}^{-1}$, but again the extreme value of 0 cross-stream GM coefficient was used.

As in the 0.2° runs, there is no tapering at all of the

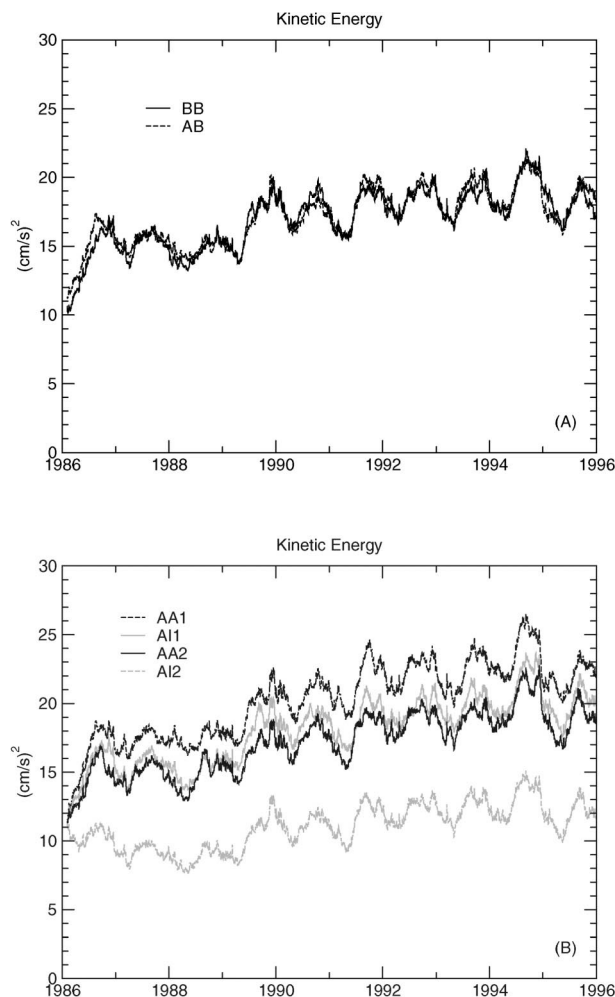


FIG. 1. Time series of global-mean total kinetic energy: (a) runs BB and AB; (b) runs AA1, AI1, AA2, and AI2.

biharmonic diffusion coefficient in case B, but tapering is applied to the GM coefficient in case A. The tapering for steep slopes is the same as described above. The upper-ocean tapering is only applied at depths shallower than the boundary layer depth diagnosed from the KPP vertical mixing scheme. This again leads to some noise in the upper ocean and the deep convection regions, and so, as was done in the 0.2° cases, we conducted a branch run starting in February 1996 of run A, called run A', in which isopycnal diffusion is replaced with horizontal mixing in the mixed layer (see section c of the appendix). This was again successful in eliminating noise without otherwise degrading the solution, as will be discussed below. We recommend that future runs at 0.1° resolution use horizontal tracer diffusion where the GM scheme is turned off, to control this noise.

4. 0.2° simulations of the North Atlantic Ocean

Several aspects of the North Atlantic simulations at 0.2° are compared and contrasted in this section.

TABLE 2. Basin-averaged mean (MKE) and eddy (EKE) kinetic energies ($\text{cm}^2 \text{s}^{-2}$) averaged over the 3-yr period of 1993–95 for the 0.2° runs and 1998–2000 for the 0.1° runs.

Run	MKE	EKE	Total
BB	6.38	12.16	18.54
AB	6.34	12.30	18.64
AA1	8.19	14.38	22.57
AI1	8.05	12.15	20.20
AA2	7.59	11.55	19.14
AI2	6.54	5.84	12.38
AI1'	7.73	12.06	19.79
AA2'	7.45	11.28	18.73
B	10.00	26.37	36.37
A	10.64	24.22	34.86
A'	10.62	23.70	33.32

a. Kinetic energy

It is well known that isotropic harmonic viscosity with a coefficient large enough to control numerical noise overly damps the eddy field in the eddying regime, which is why biharmonic viscosity is preferred. Figure 1a shows the timeseries of globally averaged total kinetic energy (KE) from runs BB and AB. It is clear that anisotropic viscosity, used in AB, allows the KE level to be as high as in the biharmonic viscosity case, BB. These two cases also have almost the same partition into mean KE and eddy KE. This can be seen in Table 2, which shows the globally averaged mean and eddy KE averaged over 1993–95 for all the 0.2° runs.

Table 2 also shows that the eddy KE is increased considerably in the anisotropic GM runs, AA1 and AA2, in comparison with the isotropic GM runs, AI1 and AI2. The increase in eddy KE is 98% when the large coefficient, $500 \text{ m}^2 \text{ s}^{-1}$, is used but is much smaller at 18% when the small coefficient, $50 \text{ m}^2 \text{ s}^{-1}$, is used. The time series of total KE from these four cases are shown in Fig. 1b. It shows that the KE levels are comparable in the cases AA1, AI1, and AA2, although the anisotropic case with the small coefficient, AA1, has the most energy. In fact, the solutions from these three cases are very similar in many respects, as will be described throughout this section. The outlier in the four GM runs is AI2, which uses isotropic GM with the large coefficient. Table 2 shows this run has a lower mean KE and a much smaller eddy KE, which is characteristic of lower-resolution runs where the eddy field is overly damped. To overcome this damping of the eddies was a prime motivation for developing the anisotropic GM parameterization.

b. Sea surface height

The mean sea surface height (SSH) for the period 1993–95 from runs AA2 and AI1 is shown in Fig. 2. The patterns are very similar in these two cases, and are not much different in runs BB, AB, and AA1. The only case that shows a significantly different mean SSH

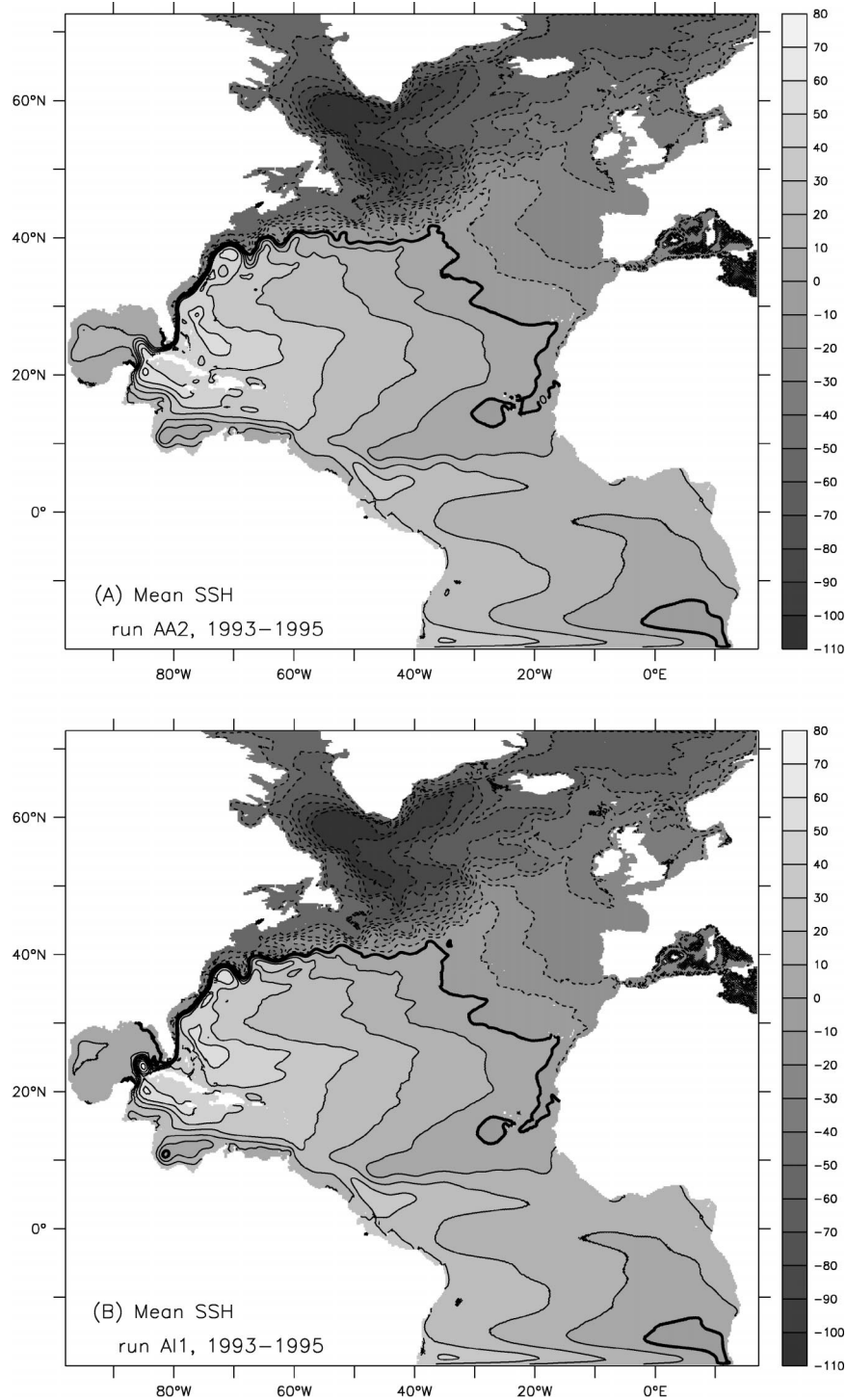


FIG. 2. Mean sea surface height for 1993–95: (a) run AA2 and (b) run AI1.

pattern is the strong isotropic run AI2 (not shown), where the flow is much more laminar, reminiscent of coarser-resolution non-eddy-resolving solutions. The only significant difference in Fig. 2 is that in run AI1 there is a persistent standing eddy in the loop current

in the Gulf of Mexico northwest of Cuba. This is unphysical because it is not seen in observations. In fact, it occurs in both cases with the small GM coefficient, but is absent in both cases with the large coefficient, suggesting that the small coefficient is too small to rep-

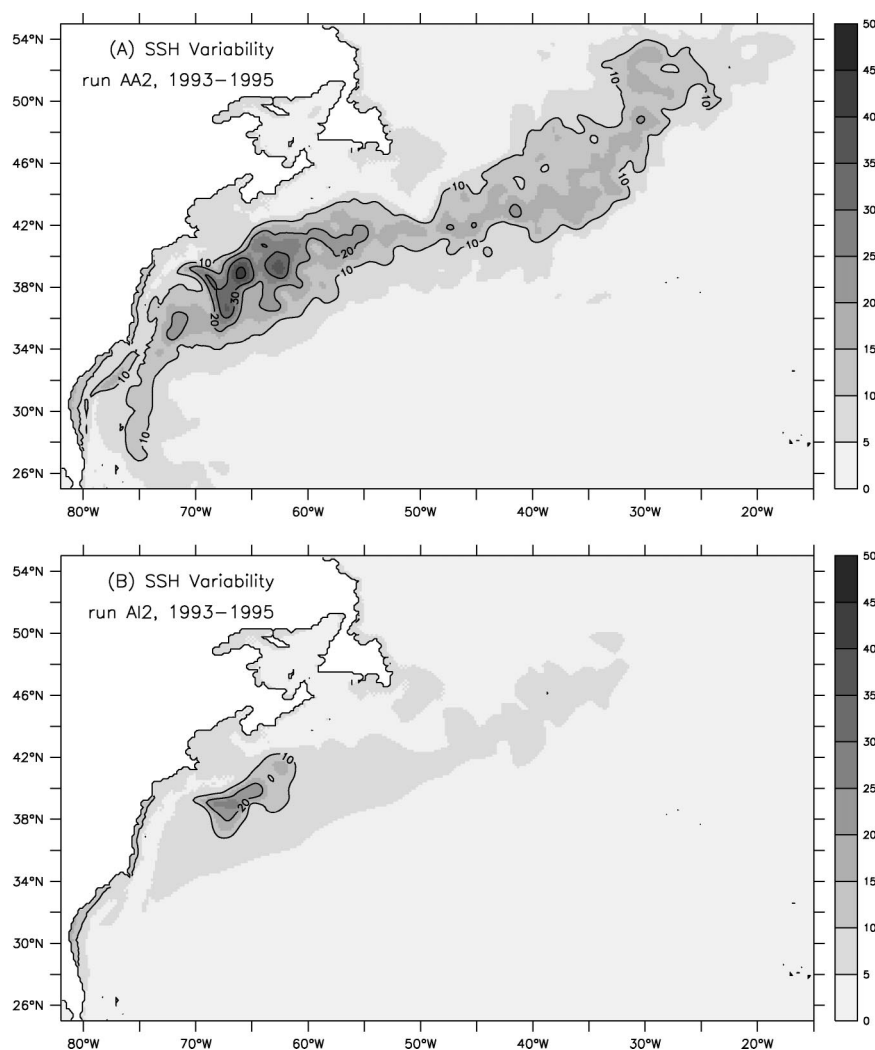


FIG. 3. Sea surface height variability for 1993–95 in the Gulf Stream and North Atlantic Current: (a) run AA2 and (b) run AI2.

resent adequately the unresolved eddy diffusion processes in this region.

This illustrates the point that in eddying simulations the mixing coefficients cannot simply be reduced to the minimum values required by the numerics, because doing so leads to unphysical aspects in the solutions. The conclusion is that, even in the eddy-resolving regime, the solutions are sensitive to the parameterizations, and subgrid-scale processes must be adequately parameterized. This point is illustrated in more detail in the companion paper by BHS.

The SSH variability for the period 1993–95 from runs AA2 and AI2 is shown in Fig. 3. The variability from the other four runs (BB, AB, AA1, AI1) is not shown but is similar to the AA2 run shown in Fig. 3a. The regions of largest SSH variability are in the Gulf of Mexico and in the Gulf Stream along the North America coast east to about 50°W. There is weaker SSH variability farther to the east as the North Atlantic Current

heads northeast across the basin. It is important to note that all the 0.2° solutions shown here fail to produce a realistic path for the North Atlantic Current, which should turn northward around the Grand Banks. In addition, all the 0.2° solutions have a very weak, or non-existent Azores Current, which should be present in the central and eastern basin at about 35°N. A much better simulation of the Gulf Stream, the North Atlantic Current, and the Azores Current was obtained in the 0.1° simulations of SMBH. Thus, the anisotropic viscosity and GM parameterizations do not solve some fundamental problems with the mean circulation in North Atlantic 0.2° solutions, and evidently higher spatial resolution is required to do so.

Figure 3b shows that the SSH variability in the AI2 case is very small as compared with the other cases. The majority of the SSH variability in the Gulf Stream has disappeared in the strong isotropic GM case. In fact, the SSH variability is reduced everywhere north of

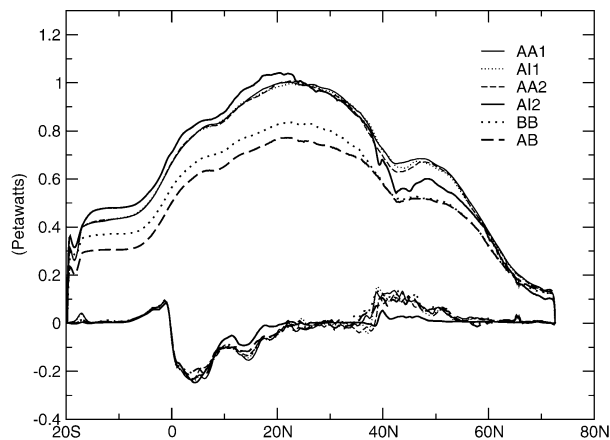


FIG. 4. Mean northward heat transport from all 0.2° runs for 1993–95. Upper curves show the total heat transport, and lower curves show the contribution from eddy heat fluxes.

20°N , even in the quieter regions of the central and eastern North Atlantic, demonstrating that the AI2 run is much more laminar, similar to coarser-resolution non-eddy-resolving solutions.

c. Heat transport and overturning circulation

The northward heat transport averaged over 1993–95 from all six 0.2° runs is shown in Fig. 4. The lower curves show the eddy heat transport, and the upper curves show the total (mean plus eddy). This is the heat transport due to advection but does not include the contribution from the eddy-induced velocity \mathbf{u}^* . However, this latter transport is very small in the North Atlantic Ocean [see the diagnostic calculation in Gent et al. (1995)]. The northward heat transport is larger in all the cases using GM than in the BB and AB runs, which use biharmonic tracer diffusion. The maximum transport in all the GM runs is about 1 PW and is 1.2 times as large as in the BB and AB runs. The heat transport at 24°N in the GM runs is consistent with the estimate by Hall and Bryden (1982) using observations, which is 1.2 ± 0.3 PW. This increase in the maximum North Atlantic heat transport is a ubiquitous feature of solutions in which horizontal tracer diffusion is replaced by the GM scheme. It has been documented at all resolutions from the non-eddy-resolving regime (see Danabasoglu and McWilliams 1995) to the high-resolution, eddying regime as shown in this work (see section 5c).

Note also from Fig. 4 that the heat transport in the AI2 run is a little different than the other GM runs. The northward heat transport is slightly stronger south of 20°N and slightly weaker north of 40°N . Much of this difference can be accounted for by weaker eddy heat transports between 10° and 20°N and between 40° and 50°N . In the latter region, the other GM runs all have a transport of about 0.1 PW by transient eddies. The only other place where transient eddy transport is significant is between 0° and 10°N , where the tropical in-

stability waves produce a maximum equatorward transport of about 0.2 PW in all six 0.2° experiments.

The meridional overturning circulation from the mean flow, averaged over 1993–95 from runs BB and AA2 is shown in Fig. 5. The overturning circulation is considerably stronger in AA2, with maxima of 17.4 Sv ($1 \text{ Sv} \equiv 10^6 \text{ m}^3 \text{ s}^{-1}$) at 35° and 43°N as compared with 13.5 Sv at 44°N in BB. The overturning penetrates more deeply in AA2, with the 2-Sv contour crossing 25°N at 3.6-km depth as compared with only 3 km in BB, and there is a larger transport across the equator in AA2. This is all consistent with the elimination of the Veronis effect (Veronis 1975) when the GM parameterization is used. The stronger meridional overturning circulation is the direct cause of the larger northward heat transport in the GM cases shown in Fig. 4. Böning et al. (1996) have shown a very good linear relationship between the maximum heat transport in the North Atlantic and the strength of the overturning circulation at about 24°N .

The meridional overturning streamfunctions from the other cases are not shown, but in AB the overturning is slightly weaker than in BB, consistent with the slightly reduced northward heat transport in Fig. 4. The overturning circulations in the other GM cases are all similar to AA2, except that AI2 has a very slightly stronger overturning near 20°N , consistent with the slightly larger heat transport at this latitude.

d. Deep-water transport

Figure 6 shows the transport of water in the 2° – 3°C potential temperature class from the BB and AA2 runs. The scale given by the colors is Sverdrups per 100 kilometers, and so the units give what the transport would be if the current were 100 km wide, and the arrows represent the flow direction. Figure 6 shows that, in this water class, there is a big difference between the two solutions. The GM case, AA2, has a much better defined and stronger deep western boundary current along the east coast of Greenland and in the Labrador Sea than the biharmonic case BB. It also flows around the Grand Banks, and connects with the deep western boundary current beneath the Gulf Stream. The stronger and colder deep current in the GM case, AA2, is consistent with the different meridional overturning streamfunctions shown in Fig. 5. It is also consistent with what was found using GM in non-eddy-resolving solutions (see, e.g., Danabasoglu and McWilliams 1995). These features of the GM run are almost certainly more realistic. The transport in this temperature class in the AB run is very similar to that in BB shown in Fig. 6a. This makes it very clear that this improvement in deep transport is due to the use of the anisotropic GM, rather than the anisotropic viscosity.

e. Convection in the Labrador Sea

The Labrador Sea is a region of the world's oceans where deep convection occurs. Thus, the isopycnals are

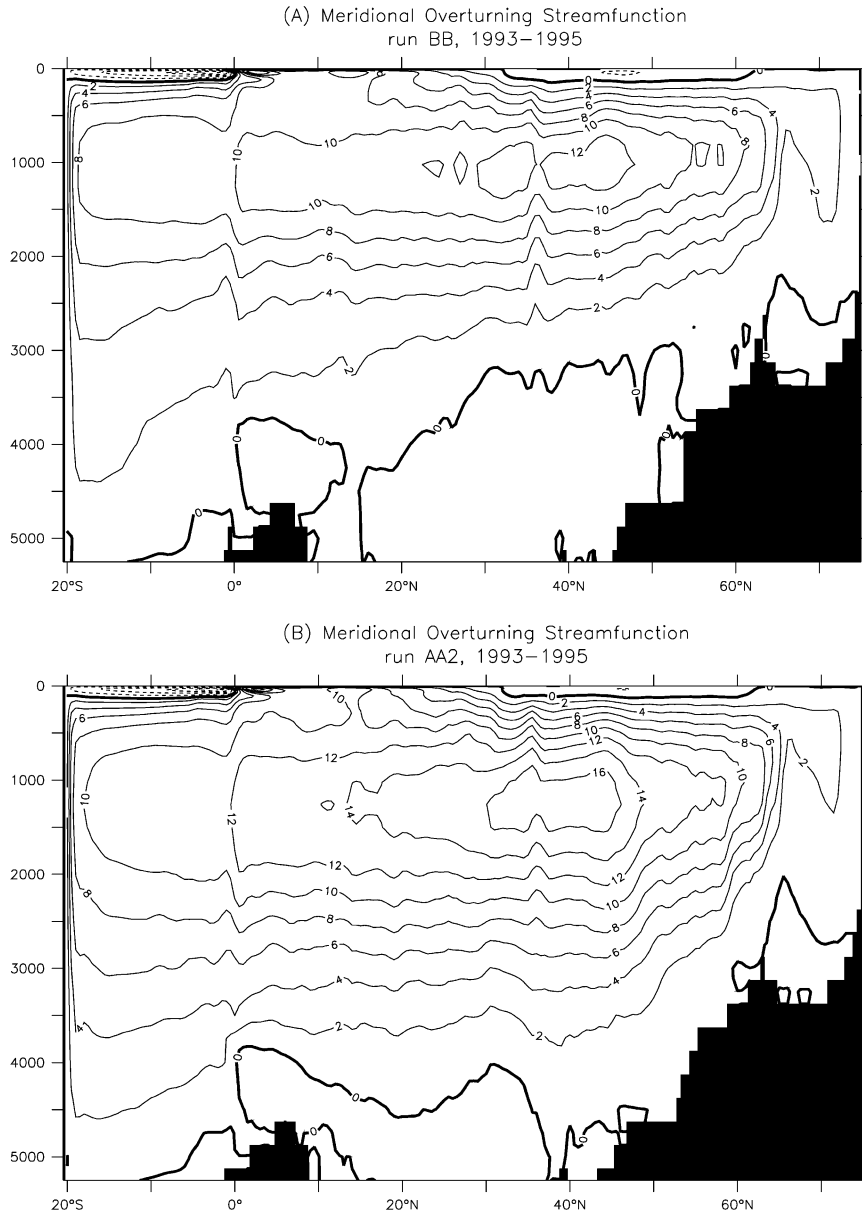


FIG. 5. Mean meridional overturning streamfunction from the mean flow for 1993–95: (a) run BB and (b) run AA2.

often very steep, which means that the GM tapering functions described in section 3a will operate much more often than elsewhere in the model domain. This results in a significant amount of numerical noise in this region in all the solutions using GM. This is shown in Fig. 7a, which shows the SST in the northwest Atlantic on 27 March 1995 from run AA2. Considerable numerical noise is seen both in the Labrador Sea and in the Gulf Stream Extension where there are very strong SST gradients.

Figure 7b shows the same plot, but from run AA2'. In this run, GM is replaced by horizontal harmonic diffusion where the GM tapering occurs, as described in

section 3a. The figure shows that the numerical noise in the SST is reduced to an acceptable level while the overall SST pattern is almost the same as in run AA2. This is also true for all the fields that have been described so far in this section; the AA2 and AA2' runs have very similar solutions. Thus, run AA2' is deemed a success because of the greatly reduced numerical noise. The noise is also significantly reduced in run AI1' when compared with run AI1 (not shown). However, the small isotropic GM coefficient still results in fairly high levels of SST noise even when horizontal diffusion is added in the upper ocean. This leads us to conclude that the best approach is to use anisotropic GM in the

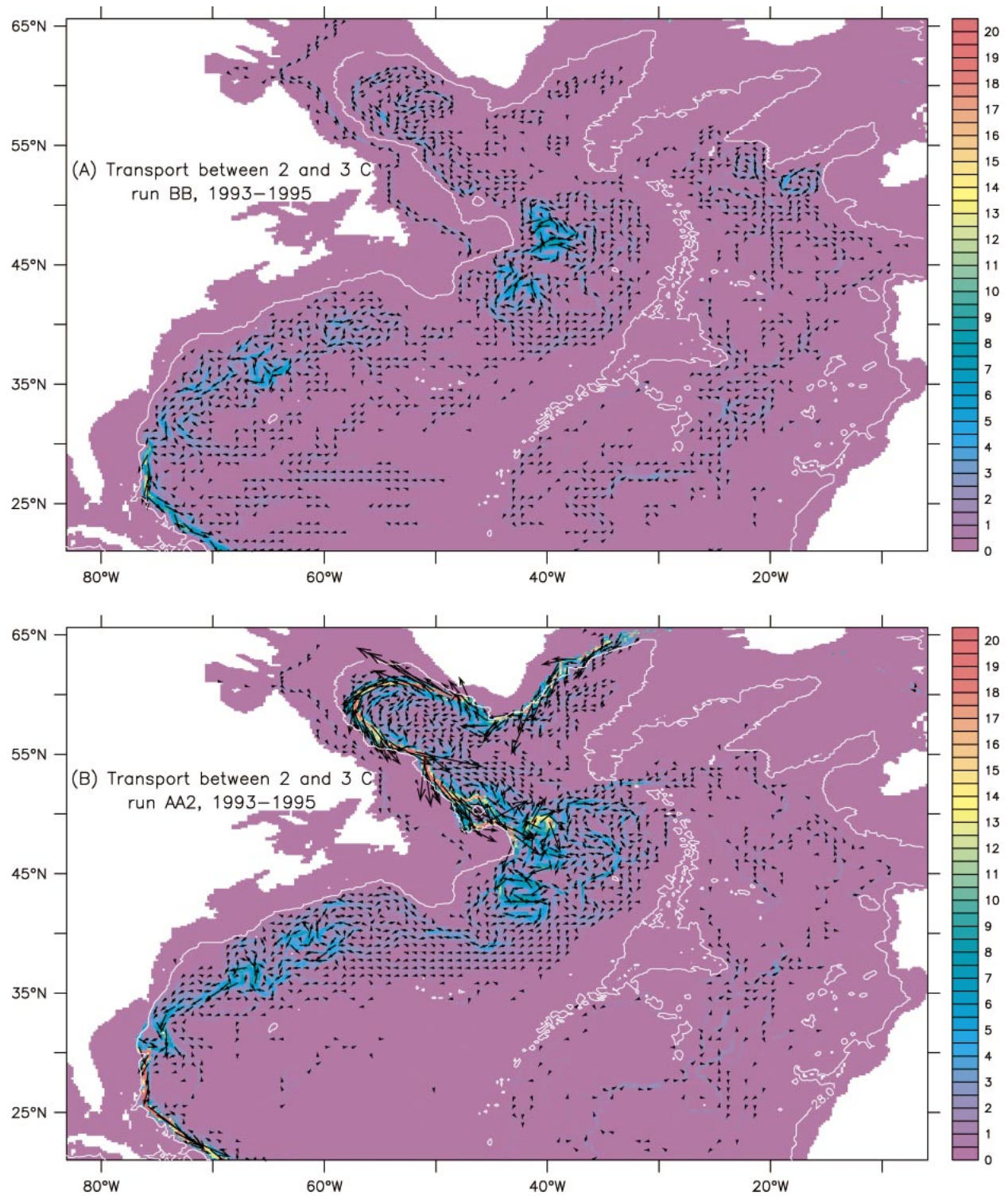


FIG. 6. Deep transport in the 2°C–3°C class averaged over 1993–95: (a) run BB and (b) run AA2. The colors show the magnitude of the flow, and arrows show its direction. The color bar is cut off at 20 Sv (100 km)⁻¹, and so all transports stronger than that value are shown in orange.

interior and horizontal mixing in the mixed layer, with an along-stream diffusivity sufficiently large to control numerical noise.

Figure 8 shows a vertical cross section of potential density referenced to the surface along 53°W on 26 March 1995 from runs BB and AA2'. The same plots from runs AB and AI1' (not shown) are very similar to those from run BB and run AA2', respectively. This confirms that the large differences shown in Fig. 8 are due to replacing biharmonic tracer diffusion by anisotropic GM. The main difference is that the density in the deep Labrador Sea is considerably greater in run AA2', so that the top to bottom density gradient is much stronger in the GM run. The denser deep water is consistent with the enhanced deep transports in the GM runs described in the previous subsection, and with previous results using GM in non-eddy-resolving models (e.g., Hirst and McDougall 1996; Large et al. 1997).

The larger top to bottom density gradient using GM is more realistic compared to recent observations made in the Labrador Sea deep convection experiment. Figure 8 of Pickart et al. (2002) and Fig. 11 of Cuny et al. (2002) show four cross sections from the Labrador Sea taken in October 1996, and February, March, and May 1997. The bottom densities are all slightly greater than 27.9 sigma units, which is consistent with the GM runs. The surface densities in early 1997 from observations are somewhat less dense than those in the GM runs. This could be year-to-year variability, but it should be noted that in all the 0.2° runs the salinities in the upper Labrador Sea are greater than in observations. Thus, the top-to-bottom density gradient in reality is somewhat larger than in the GM run AA2' shown in Fig. 8b. However, the GM runs give a much more realistic density profile in the Labrador Sea than do the runs using biharmonic tracer diffusion.

5. 0.1° simulations of the North Atlantic Ocean

In this section the 0.1° simulations with anisotropic and biharmonic mixing are compared. Essentially all of the features and improvements seen in the anisotropic cases when compared with the biharmonic cases at 0.2° described above carry over to the 0.1° runs. The time series of total KE in the biharmonic run B and anisotropic run A (not shown) are very similar. The mean, eddy, and total KE, averaged over 1998–2000, are given in Table 2. The ratio of eddy KE to mean KE for this period is 2.6 and 2.3 in runs B and A, respectively. In addition to the type of improvements seen in the 0.2° anisotropic GM cases, the 0.1° anisotropic run A also shows improvements in the mean circulation that will be described below.

a. Gulf Stream path

Figure 9 shows snapshots of the Gulf Stream path from cases B and A. The figure shows instantaneous

paths of the Gulf Stream, defined by the 12°C isotherm at 400-m depth, every 10 days for the 3-yr period 1998–2000. The thick and thin solid lines in the middle indicate the mean path and the meander envelope, defined as 1 standard deviation in the latitudinal position of this isotherm. The northern solid lines with perpendicular bisections show the same from the Watts et al. (1995) observations between 75° and 67°W. More details on this type of figure can be found in section 3c of SMBH. Figure 9 shows that the Gulf Stream path after separation is too zonal in both runs as compared with observations, but case A is an improvement over case B. The separated jet is much tighter in run A east to about 70°W before it starts to have significant meanders. This is in better agreement with the observations than for case B, where the meanders start at 74°W. Also, the width of the meander envelope is narrower in case A between 75° and 65°W than in case B, again in better agreement with the observations. The downstream transport (not shown) between 60° and 50°W is somewhat weaker in run A than run B. This results from weaker recirculation gyres on the flanks of the Gulf Stream in the anisotropic GM run.

b. Surface height variability

The SSH variability from runs B and A averaged over 1998–2000 is shown in Fig. 10 in the region of the Gulf Stream and the North Atlantic Current. The maximum amplitude of the variability in the Gulf Stream meander region is about the same in the two runs, but Fig. 10 shows two distinct improvements in case A. The first is in the region of the northwest corner, near 50°N, 45°W, where the North Atlantic Current is seen to penetrate farther to the northwest in run A, in better agreement with satellite observations of SSH variability (see Fig. 17c of SMBH). Second, the Azores Current at 35°N in the central and eastern basin is much better defined in run A than B, as shown by the increased SSH variability associated with that current east of 45°W. In run A the mean transport averaged from 1998–2000 between 35° and 25°W is about 10 Sv, which compares quite well to an observational estimate of 10–15 Sv by Käse and Krauss (1996). It should be noted that improvements similar to these were also obtained in biharmonic runs at 0.1° using lower values of the mixing coefficients (see the companion paper, BHS). However, the improvements in the Gulf Stream jet after separation discussed in the last section were not seen in any of the biharmonic runs.

c. Heat transport and overturning circulation

Figure 11 shows the northward total heat transport (upper curves) and eddy heat transport (lower curves) from runs B and A for the 3-yr period 1998–2000. The eddy contribution is comparable in the two runs, but the

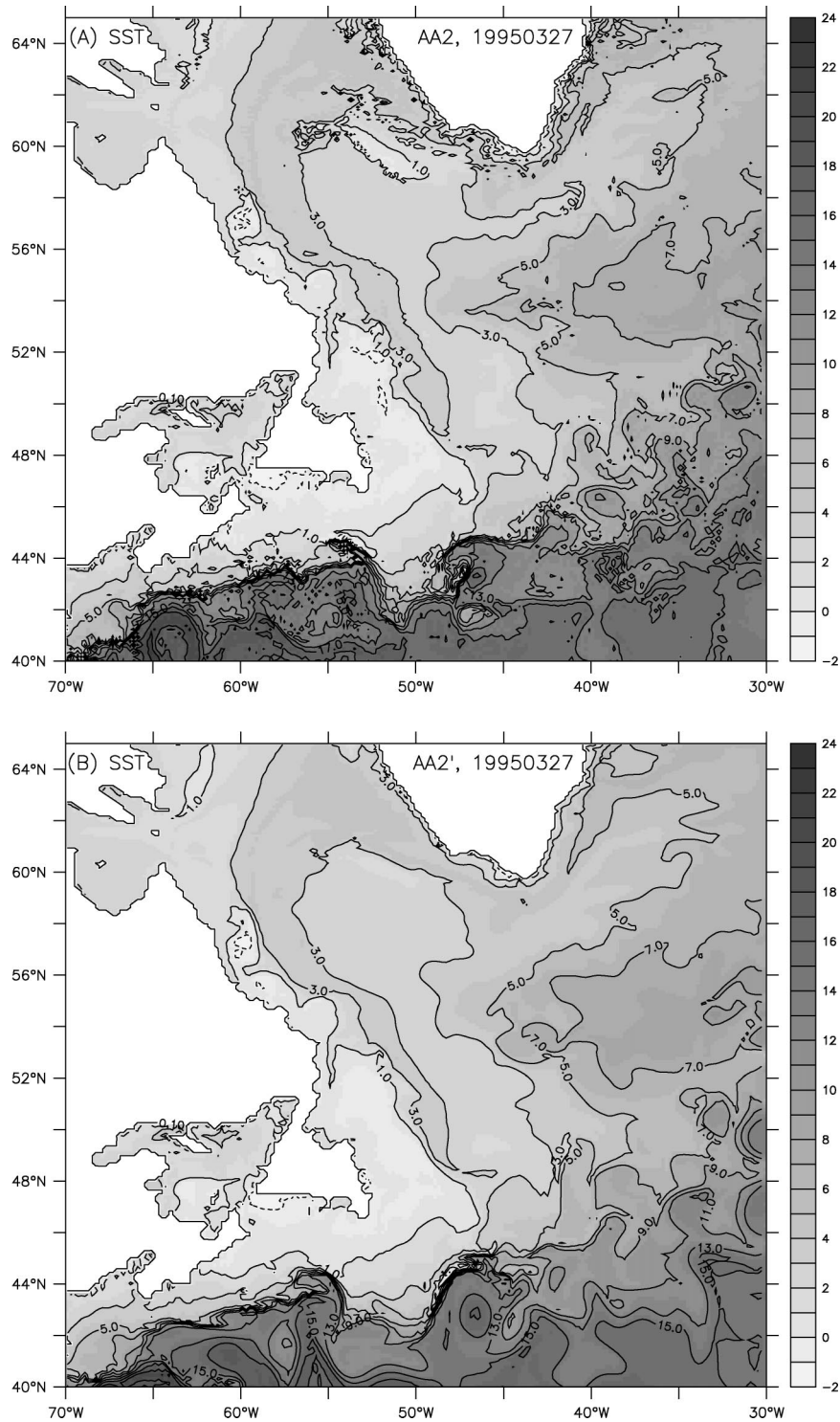


FIG. 7. SST in the northwest Atlantic on 27 Mar 1995: (a) run AA2 and (b) run AA2'.

total transport is larger in the anisotropic GM case A. The maximum at 25°N is 1.2 PW, a 11% increase over case B. These maxima are in excellent agreement with the estimate of 1.2 ± 0.3 PW by Hall and Bryden (1982). The elimination of the Veronis (1975) effect in

run A results in a 0.1-PW-larger northward heat transport from the southern hemisphere all the way to 35°N. Also shown is the heat transport from the branch run A' in which anisotropic horizontal diffusion replaced GM in the mixed layer. It is clear from the plots that

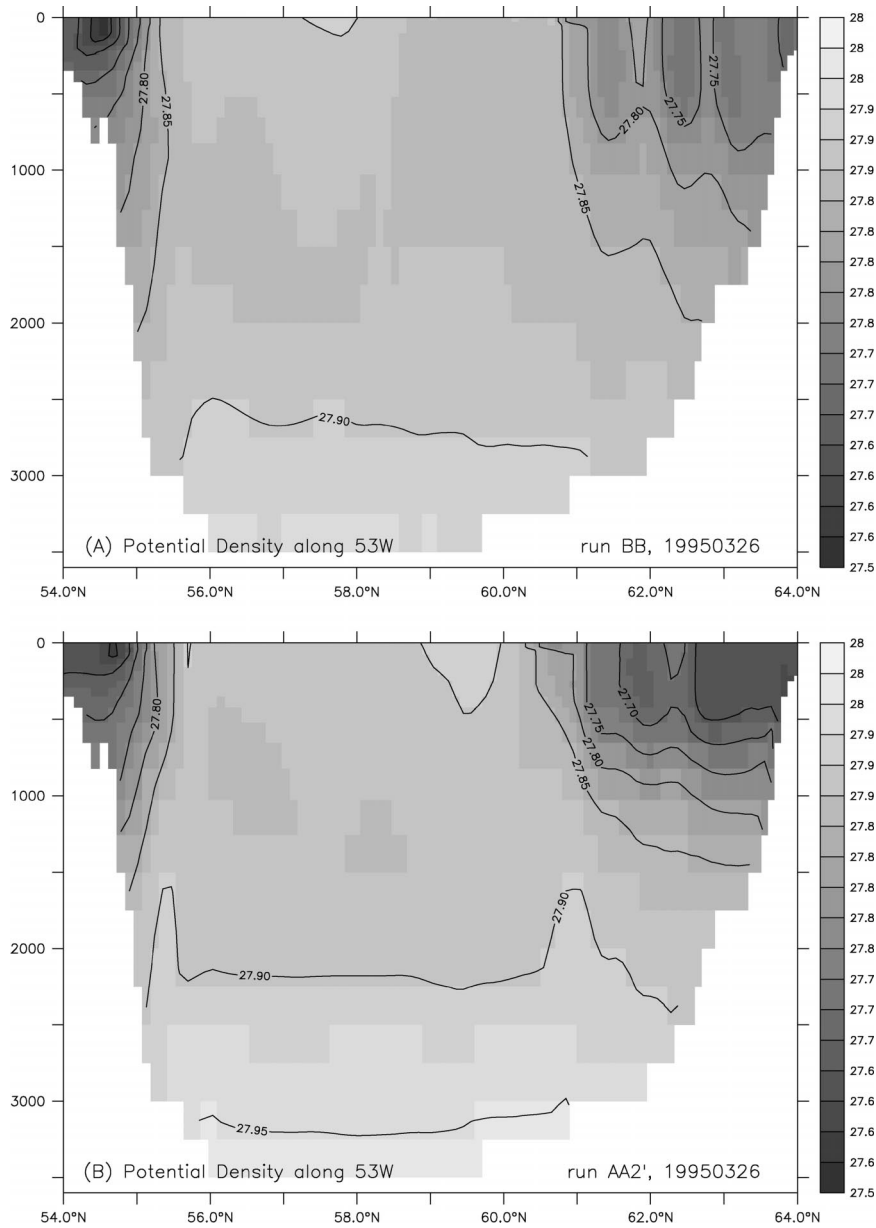


FIG. 8. Vertical cross section of potential density referenced to the surface along 53°W on 26 Mar 1995: (a) run BB and (b) run AA'.

there is very little difference between the heat transport in runs A and A'.

This is the first demonstration we know about of the beneficial effects of GM on ocean solutions in the edying regime at 0.1° resolution. Roberts and Marshall (1998) showed improvements at resolutions down to 1/8°, but only in an idealized model calculation. This increase in the maximum heat transport in the North Atlantic by GM decreases as the model resolution gets finer; it is on the order of 100% at a resolution of 3°–4° (Danabasoglu and McWilliams 1995), about 20% at 0.2° resolution, and about 10% at 0.1° resolution. However, using GM has as large an effect at 0.1° as at 0.2°

on some quantities, such as convection, stratification, and deep boundary currents in the Labrador Sea, as documented in the next few sections.

The meridional overturning streamfunction from the mean flow, averaged over 1998–2000 from runs B and A is shown in Fig. 12. Just as in the 0.2° runs, the increased heat transport in run A is due to a stronger overturning circulation. The maximum at 35°N, 1-km depth is 22.9 Sv in run A, as compared with 20.4 Sv at 33°N in run B, and there is stronger flow across the equator in A, resulting in a larger heat transport. Also, the 0 contour is at about 4-km depth in run A, whereas it is at about 3.6-km depth in run B. Thus, the North

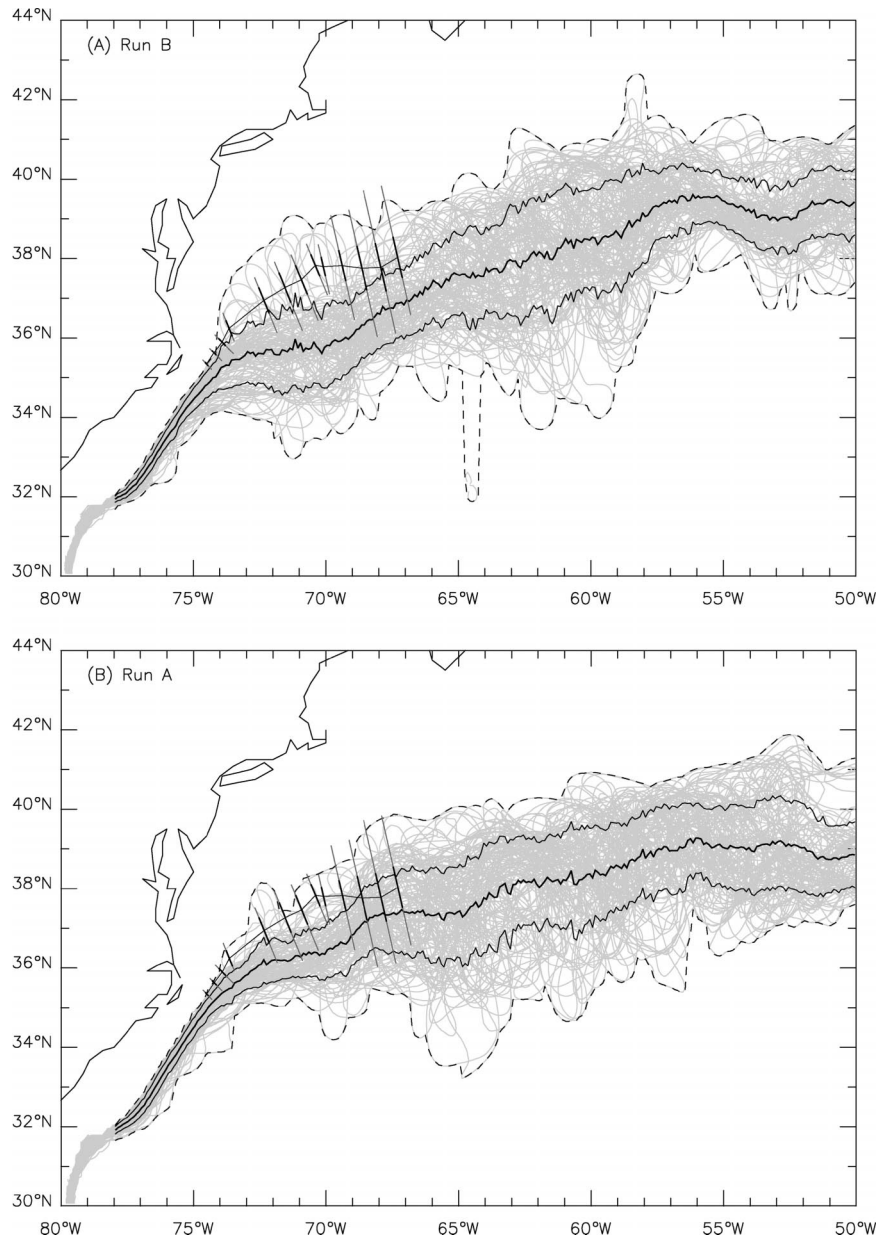


FIG. 9. Instantaneous Gulf Stream paths for 1998–2000, defined by the 12°C isotherm at 400-m depth: (a) run B and (b) run A. Solid lines in middle indicate the mean path and meander envelope, and observations from Watts et al. (1995) are shown as the solid line to the north with the perpendicular bisections.

Atlantic deep water is deeper and colder in the anisotropic GM run. This is consistent with other results implementing GM in the non-eddy-resolving regime (e.g., Hirst and McDougall 1996).

d. Deep-water transport

The deep-water transport in the 2°–3°C temperature class in runs B and A is shown in Fig. 13. Again, the colors depict the transport [$\text{Sv} (100 \text{ km})^{-1}$], and the arrows denote the average flow direction. There is al-

most no deep western boundary current in this temperature class in the Labrador Sea in run B, but a strong, coherent western boundary current is present in run A. Based on the 0.2° results in section 4, this improvement is associated with the anisotropic GM in A, and not with the anisotropic viscosity. In run A, the deep return flow east of the Grand Banks is more confined to the western half of the basin to the west of the Mid-Atlantic Ridge, whereas in run B, as well as in the 0.2° runs shown in Fig. 6, the deep return flow extends all the way east to the ridge. Also note that the two 0.1° runs have a larger

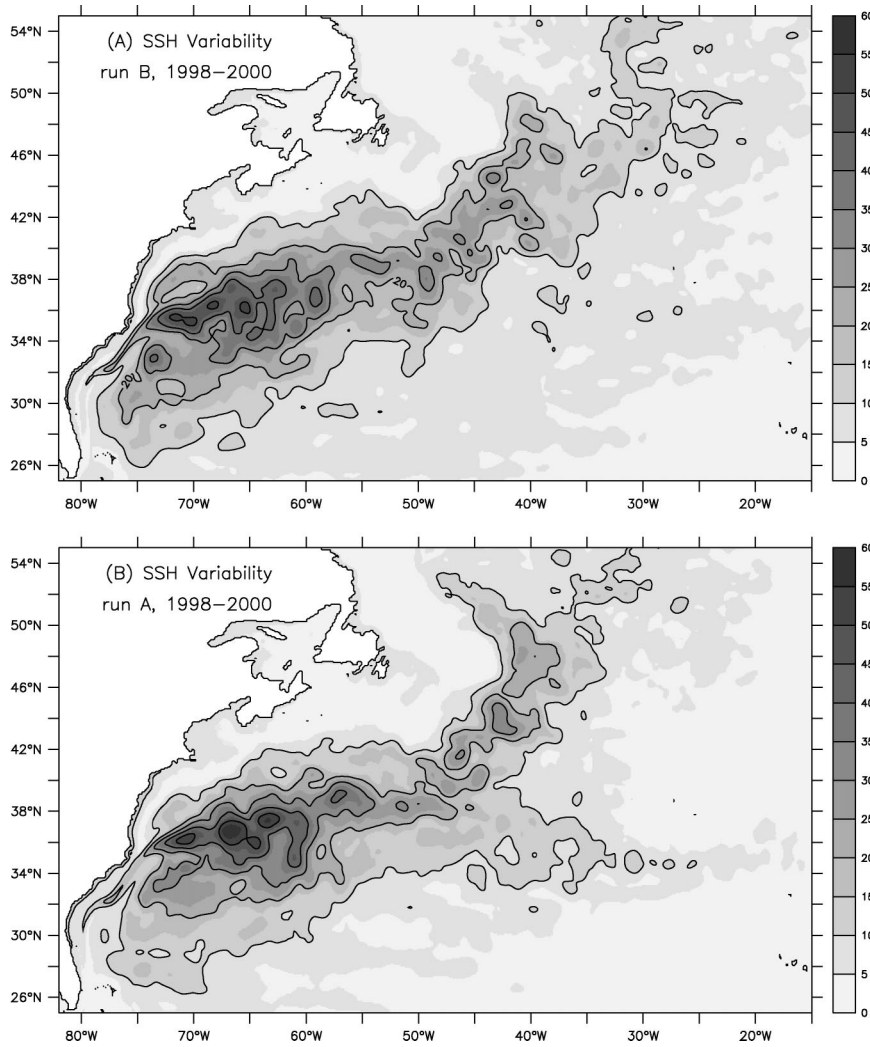


FIG. 10. Sea surface height variability during 1998–2000 in the Gulf Stream and North Atlantic Current: (a) run B and (b) run A.

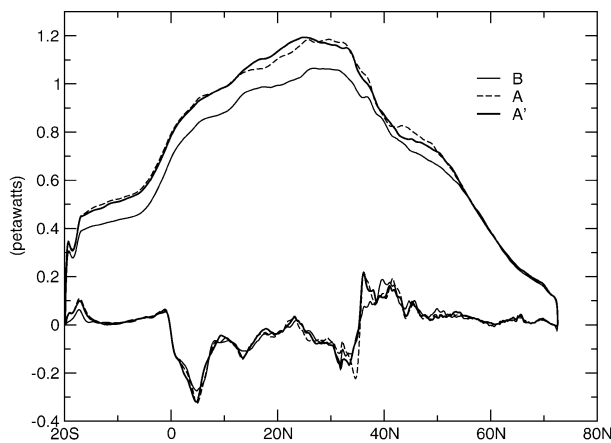


FIG. 11. Mean northward heat transport from the 0.1° runs for the period 1998–2000. Curves are as in Fig. 4.

proportion of the deep return flow rounding the Grand Banks and heading southwest than in the 0.2° runs. This return flow converges into a coherent, narrow deep western boundary current at about 30°N to the east of the Bahamas, in all runs at both resolutions.

e. Convection in the Labrador Sea

Figure 14 shows a vertical cross section of potential density referenced to the surface along 53°W on 31 March 2000 from runs B and A'. These results can also be compared with similar plots from 1995 in two 0.2° runs shown in Fig. 8. The largest difference shown in Fig. 14 is that the deep Labrador Sea is significantly denser in A' than in B by about 0.04 sigma units. Most of the upper kilometer is a little less dense in the A' run, so that its top-to-bottom density contrast is much larger than in run B. The 0.2° results show that this is due to using the anisotropic GM in A' and not from

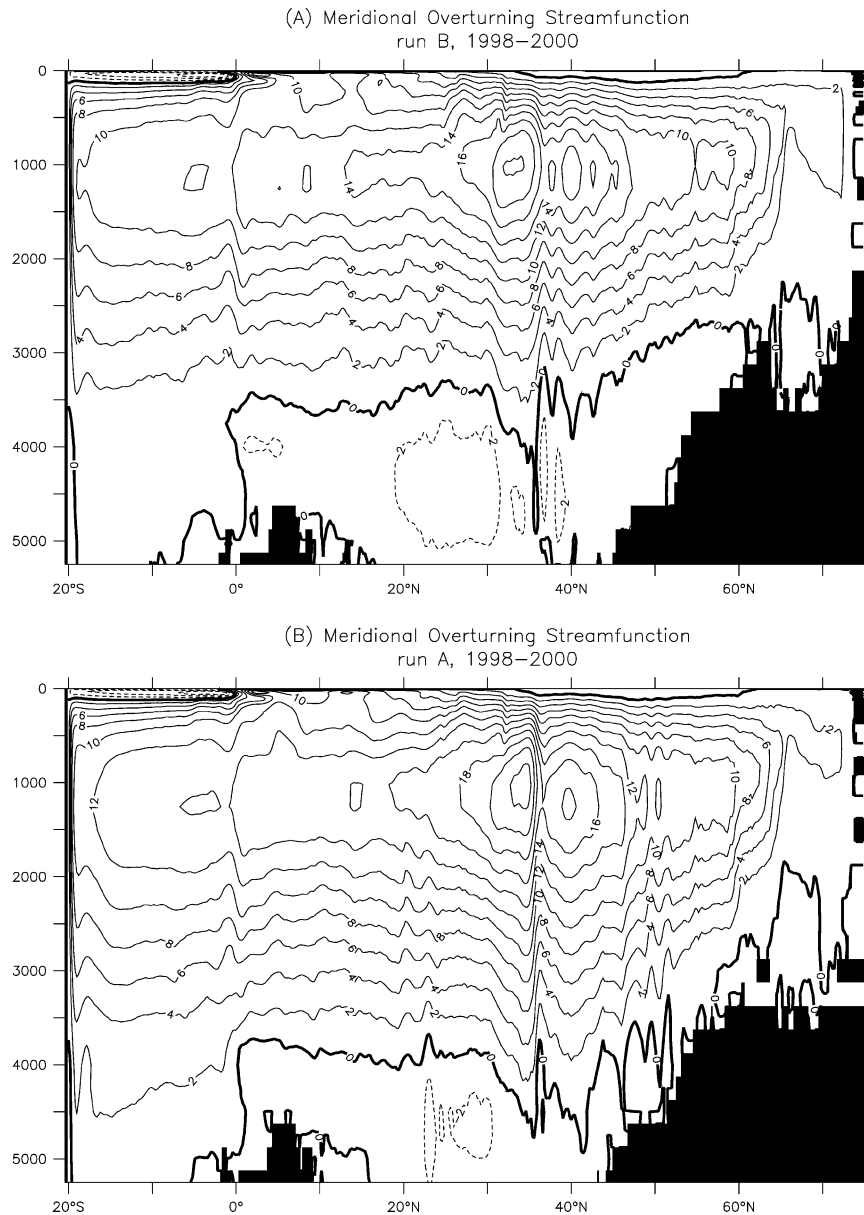


FIG. 12. Mean meridional overturning streamfunction from the mean flow for 1998–2000: (a) run B and (b) run A.

using the anisotropic horizontal viscosity. Again, comparison with the observed Labrador Sea sections in Pickart et al. (2002) and Cuny et al. (2002) shows that the A' results in Fig. 14b are much more realistic. The bottom potential temperature in A' is just above 2°C, which is much closer to the observed value of 1.4°C than in run B. The salinity values in A' are about 0.1 ppt more saline than those shown in Fig. 8 of Pickart et al. (2002), but the vertical profile is again considerably improved in run A'. In particular, the salinity maximum between 2.5- and 3-km depth is captured very well in run A'.

The much larger top-to-bottom density contrast in A'

when compared with B is very clearly manifested in the diagnosed mixed layer depth. The mixed layer depths in the Labrador Sea on 31 March 2000 from runs B and A' are shown in Fig. 15. These are diagnosed as the depth at which the potential density exceeds the surface value by 0.01 sigma units. The region of the deepest mixed layers has moved a little northwest into the central Labrador Sea in A'. However, the largest difference in Fig. 15 is that the maximum mixed layer depths are about 1.7 km in run A' as compared with 2.3 km in run B. The mixed layer depths are strongly variable in both time and space, but in the Labrador Sea they are always much shallower in run A' than in run B. Figure 2 in

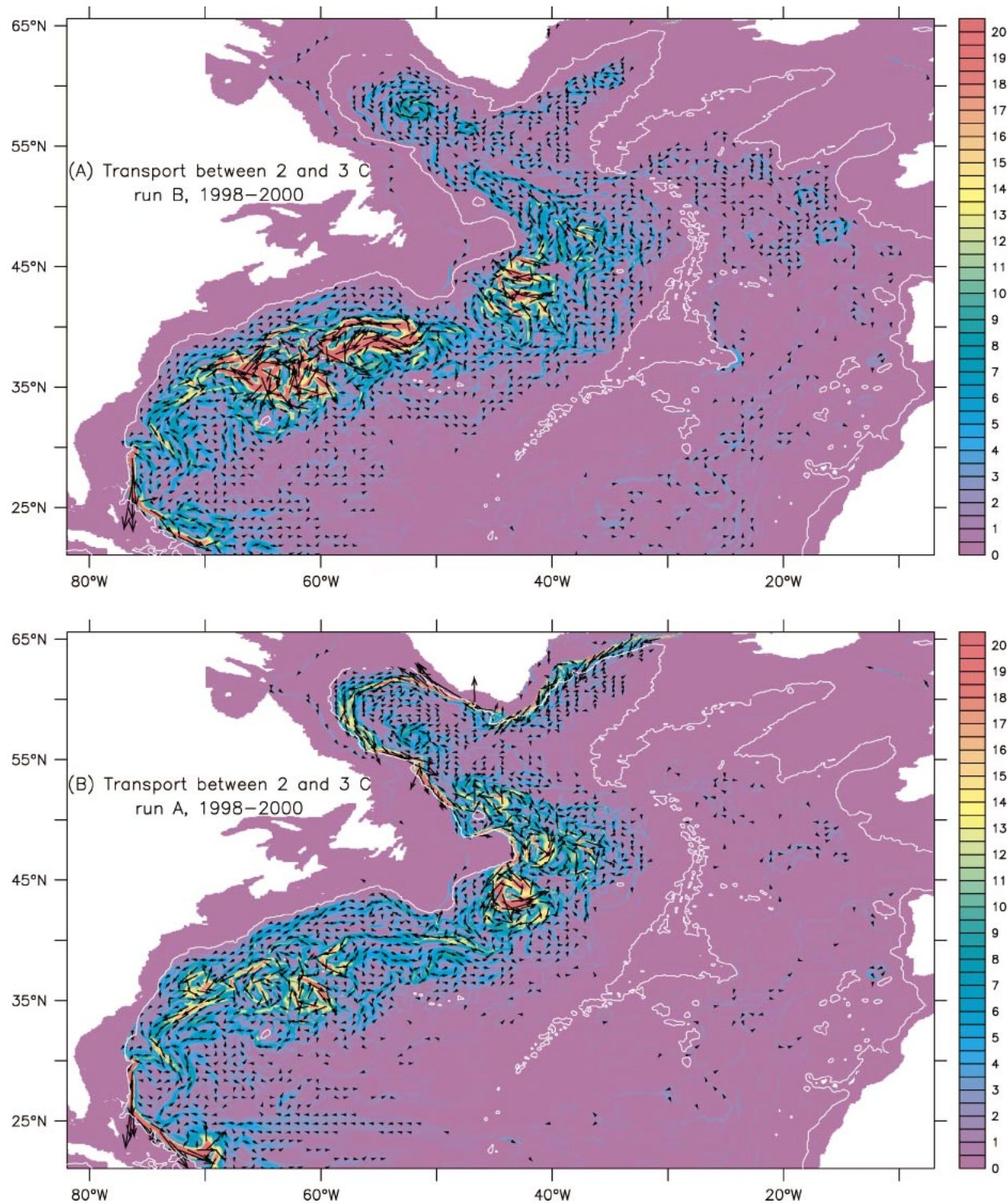


FIG. 13. The deep transport in the 2°–3°C class averaged over the period 1998–2000: (a) run B and (b) run A. Colors are as in Fig. 6.

Lavender et al. (2002) and Fig. 12 in Pickart et al. (2002) show observations of the mixed layer depth during the Labrador Sea deep convection experiment. Both show maximum mixed layer depths of about 1.3–1.4 km near

57°N, 54°W. Thus, the deep convection occurs in roughly the correct region in both runs, but the diagnosed mixed layer depth in run A' is much more realistic. As mentioned in section 4e, the near-surface waters tend

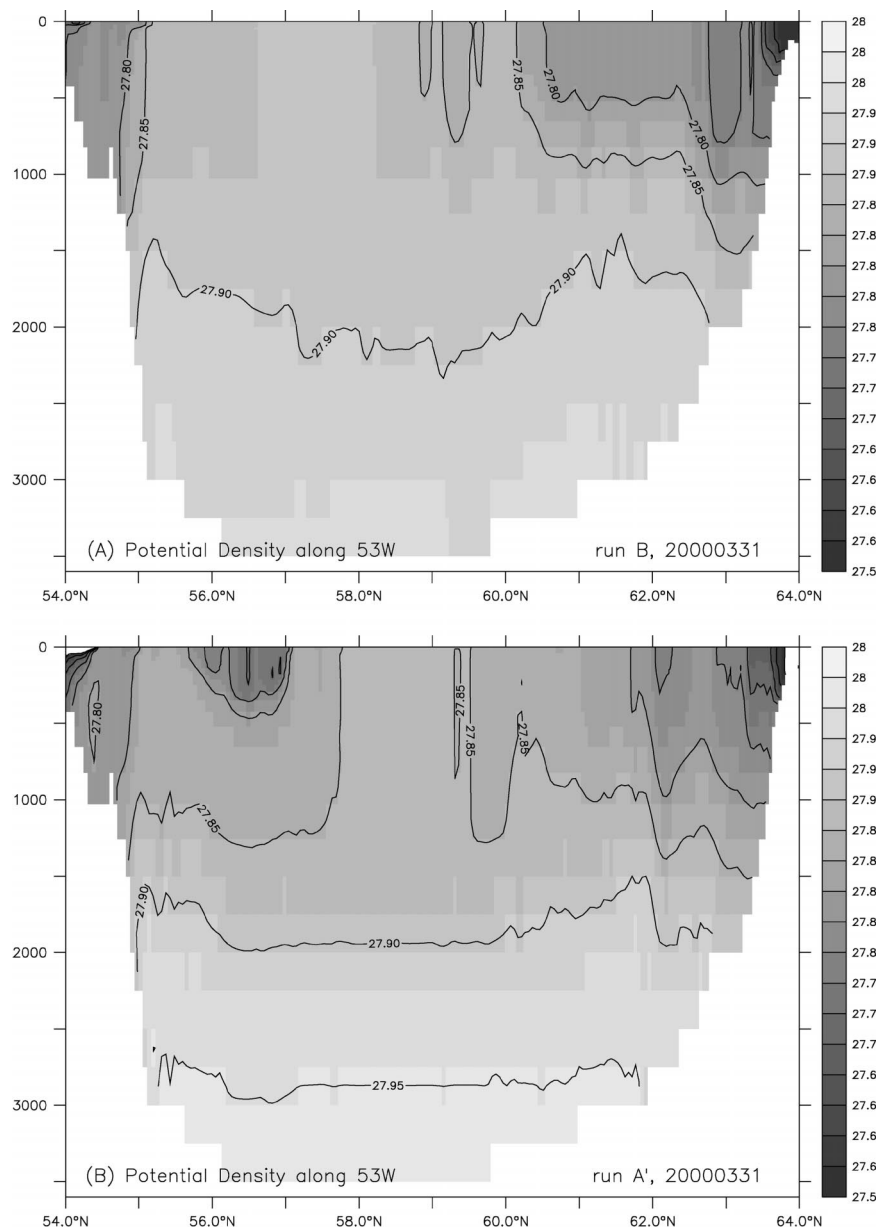


FIG. 14. Vertical cross section of potential density referenced to the surface along 53°W on 31 Mar 2000: (a) run B and (b) run A'.

to be too saline in all the model runs, so that the top-to-bottom density difference in run A' is still slightly weaker than in reality. This is likely the reason that the A' mixed layer depths are still somewhat deeper than those diagnosed from observations in the Labrador Sea.

6. Discussion and conclusions

We have developed an anisotropic generalization of the adiabatic GM parameterization and tested it, along with a complementary anisotropic viscosity parameterization, in high-resolution simulations of the North Atlantic Ocean at 0.2° and 0.1° resolution.

The anisotropic parameterizations were configured to mix tracers and momentum with relatively large along-stream coefficients, and small or 0 cross-stream coefficients. This allows for levels of eddy kinetic energy and surface height variability that are as high as can be obtained using more traditional biharmonic forms. In the limit of 0 cross-stream mixing coefficients, the anisotropic operators would have no effect on a geostrophic front with no gradient of temperature or salinity along the direction of flow, whereas isotropic diffusion would laterally diffuse such a front. In this sense the anisotropic forms can provide minimal diffusion, allowing high levels of kinetic energy and tracer variance to per-

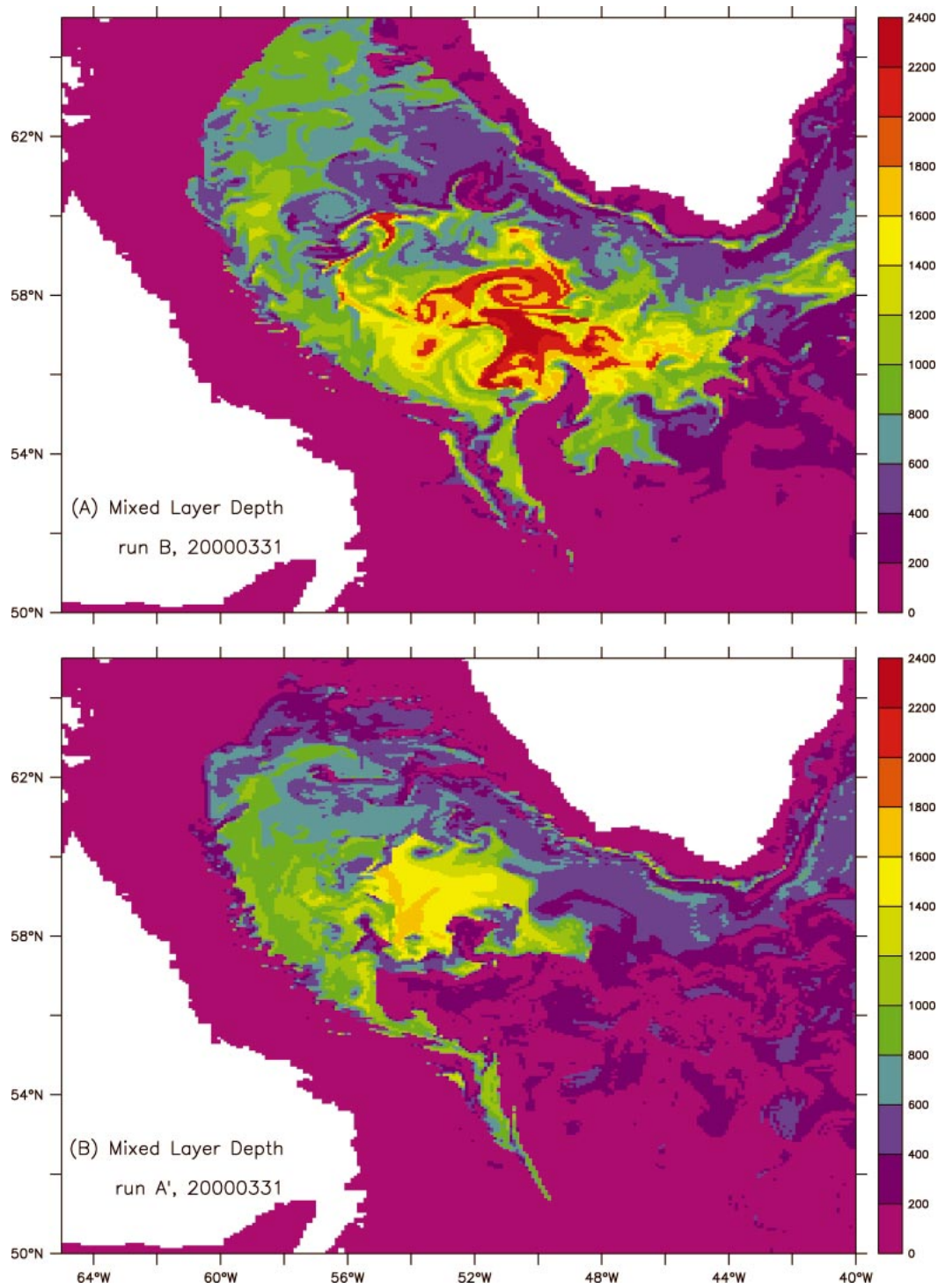


FIG. 15. Mixed layer depth in the northwest Atlantic on 31 Mar 2000: (a) run B and (b) run A'.

sist, while at the same time controlling numerical noise with sufficiently large along-stream mixing coefficients. In the 0.2° simulations, it was shown that high levels of eddy energy can also be obtained using a small isotropic GM coefficient; however, this approach resulted

in excessive noise in the solution. With a large isotropic GM coefficient this noise was not present, but the solutions were too damped and the eddy variability was greatly reduced. Furthermore, we were able to run with a 40%-larger time step using anisotropic GM with the

large along-stream coefficient (run AA2') than when using isotropic GM with the small coefficient (run AII'). The anisotropic GM routine is somewhat computationally expensive, however, taking about 29% of the total run time as compared with 23% for the isotropic GM routine.

Improvements in the mean circulation that have been seen in previous eddying 0.1° simulations of the North Atlantic using biharmonic closures, such as the Gulf Stream separation, the path of the North Atlantic Current around the Grand Banks, and the representation of the Azores Current, were retained using the anisotropic GM and viscosity parameterizations. Some additional improvements beyond what was seen in the biharmonic runs were also seen in the path and meander envelope of the Gulf Stream jet after it separates from the coast.

Improvements in the thermohaline circulation using the GM closure scheme that have been documented over the last decade in non-eddy-resolving ocean general circulation models carry over to the eddying, high-resolution simulations presented here. These include stronger meridional overturning circulation and heat transport, colder and deeper deep western boundary currents, and denser bottom water, improved stratification, and improved mixed layer depths in the Labrador Sea. These improvements are the direct result of using an adiabatic closure for the tracer transport equations, as opposed to using horizontal diffusion operators, which lead to spurious diapycnal mixing across sloping density surfaces. However, we note that spurious diapycnal mixing due to the numerical implementation of GM and due to advection schemes still occurs in z -coordinate models (Griffies et al. 1998, 2000).

When the GM parameterization is used in non-eddy-resolving simulations, the diffusivity is typically tapered to 0 in the mixed layer. In the high-resolution, eddying simulations presented here, this results in excessive numerical noise in the upper-ocean tracer fields. Applying horizontal harmonic diffusion to approximate diabatic mixing in the mixed layer was found to remove this numerical noise successfully without otherwise significantly affecting the solutions.

As discussed in the introduction, horizontal biharmonic diffusion leads to spurious diapycnal mixing of tracers and, possibly, to unphysical cabling. We conclude from the work presented in this paper that the anisotropic GM parameterization is a viable adiabatic alternative to biharmonic diffusion that is much more physically realistic. Therefore, we recommend using anisotropic GM, combined with horizontal diffusion in the mixed layer, in high-resolution ocean models.

Last, we note that the anisotropic GM parameterization has potential application in non-eddy-resolving models, as well as in the eddying models used in this work. Before this is done, however, analysis of high-resolution, eddying solutions would have to be performed to see whether the effects of eddies on the mean tracer distributions really are anisotropic in a preferred

direction. As in this work, the anisotropic GM would be used in conjunction with anisotropic viscosity, which prevents excessive lateral diffusion of equatorial currents and western boundary currents, such as the Gulf Stream. In addition, the cross-stream diffusion could be increased in open-ocean currents where lateral eddy fluxes are expected to be large. Other potential applications in non-eddy-resolving models include enhanced mixing along contours of constant latitude or f/H , as discussed in the introduction.

Acknowledgments. We thank Frank Bryan and Matthew Hecht, who participated in the design and execution of a suite of 0.1° North Atlantic simulations, including the 0.1° runs discussed in this paper. They also assisted in preparing Figs. 8, 9, 14, and 15. Further analysis of the 0.1° North Atlantic experiments can be found in the companion paper by Bryan et al. (2004, unpublished manuscript). LANL is sponsored by the U.S. Department of Energy.

APPENDIX

Functional Discretization of the Diffusion Operator

Here we derive the spatial discretization of the isopycnal diffusion and eddy-induced advection terms in the tracer transport equations for use in general orthogonal curvilinear coordinates on the sphere as they are implemented in the POP model. This method is based on an anisotropic generalization of the functional discretization of the isotropic GM diffusion operators currently used in z -coordinate ocean models (Griffies et al. 1998; Smith and Gent 2002).

a. Discretization

The discrete functional is defined by

$$\mathcal{G}(\phi) = \frac{1}{2} \sum_{ijk} \sum_{n=1}^8 v_{ijkn} (K_{xx} \phi_{\tilde{x}}^2 + K_{yy} \phi_{\tilde{y}}^2 + 2K_{xy} \phi_{\tilde{x}} \phi_{\tilde{y}})_{ijkn}, \quad (\text{A1})$$

where the tildes on the subscripts denote isopycnal derivatives of ϕ (e.g., $\phi_{\tilde{x}} = \phi_x + L_x \phi_z$). The quantity in parentheses in (A1) depends on the values of K_{ij} , ϕ_x , ϕ_y , ϕ_z , L_x , and L_y in each subcell. These gradients are discretized as differences across cell faces, and for this reason it is convenient to subdivide each full cell into eight subcells by passing planes aligned with each of the three coordinate directions through the exact center of the full cell. The subscripts (i, j, k) in (A1) run over all full cells, and the subscript n runs over the eight subcells within a given full cell. $v_{ijkn} = V_{ijk}/8$, where V_{ijk} is the volume of the full cell.

The diffusion operator is then given by the derivative of the discrete functional with respect to the field ϕ at a given point (i, j, k) :

$$\mathcal{D}_{ijk} = -\frac{1}{V_{ijk}} \frac{\partial}{\partial \phi_{ijk}} \mathcal{G}(\phi). \quad (\text{A2})$$

When taking the derivative with respect to ϕ_{ijk} , there will be contributions from the 8 central subcells surrounding the point (i, j, k) , as well as from the 24 neighboring subcells that are adjacent to the six faces of the full cell. We follow Griffies (1998) and discretize $\mathcal{B}(\phi)$ in (15) in the same way as the contribution to $\mathcal{D}(\phi)$ from the off-diagonal elements of \mathbf{K}_3 in (10). The discretization of the full operator $\mathcal{D}(\phi) + \mathcal{B}(\phi)$ is given by

$$\begin{aligned} & V_{ijk} (\mathcal{D}_{ijk} + \mathcal{B}_{ijk}) \\ &= \Delta_x \left\{ \frac{1}{h_x} \overline{v(K_{xx}\phi_x + K_{xy}\phi_y)} \right\} \\ &+ \Delta_y \left\{ \frac{1}{h_y} \overline{v(K_{yy}\phi_y + K_{xy}\phi_x)} \right\} \\ &+ \Delta_z \left\{ \frac{2}{h_z} \overline{v[K_{xx}L_x\phi_x + K_{yy}L_y\phi_y + K_{xy}(L_x\phi_y + L_y\phi_x)]} \right\} \\ &+ \Delta_z \left\{ \frac{1}{h_z} \overline{v(K_{xx}L_x^2 + K_{yy}L_y^2 + 2K_{xy}L_xL_y)\phi_z} \right\}, \quad (\text{A3}) \end{aligned}$$

where the quantities in curly braces are defined on the faces of the full cell and Δ_x , Δ_y , and Δ_z denote differences between quantities on opposing faces in the x , y , and z directions. The overbars indicate that the terms, which are uniquely defined in each subcell, should be summed over the eight subcells surrounding a given face. In addition, the form of (A3) has been simplified by assuming $\mathbf{K}' = \mathbf{K}$. This is the form that is presently coded in the POP model and used in the simulations presented in this paper. The last term in (A3) has the form of vertical diffusion with an effective vertical diffusivity coefficient

$$\nu_d = (\bar{v})^{-1} \overline{v\mathbf{L} \cdot \mathbf{K} \cdot \mathbf{L}}, \quad (\text{A4})$$

where the sum is over the eight subcells surrounding the top, or bottom, face of the full cell, and $\bar{v} = Ah_z$, where A is the horizontal area of the full cell. If the isopycnal slopes are larger than the vertical-to-horizontal-cell aspect ratio dz/dx , then this term must be treated implicitly, because the vertical diffusivity can be large enough to violate explicit diffusive Courant–Friedrichs–Lewy conditions. In the code, ν_d is added to the model vertical diffusivity and the vertical diffusion is solved implicitly.

b. Boundary conditions

The boundary conditions on the diffusion operator $\mathcal{D}(\phi)$ are determined from the requirement that, in the absence of external sources and sinks, the operator conserves the volume-integrated tracer content and reduces

the mean tracer variance. Similarly, the boundary conditions on the eddy-induced transport operator $\mathcal{B}(\phi)$ are determined by requiring that it conserves the volume-integrated tracer and leaves the mean tracer variance unchanged. In the discrete operator, the boundary conditions cannot be satisfied by simply setting the fluxes normal to the boundary to 0 after summing the contributions to the fluxes from each subcell. To satisfy the global constraints, the boundary conditions must be applied within each subcell adjacent to the boundary before the contributions from the subcells are summed to form the fluxes. The simplest way to satisfy the boundary conditions in the discrete operator is to set $\mathbf{K} = \mathbf{K}' = 0$ in all subcells adjacent to the boundary. We employ this simple prescription in the calculations presented in this paper.

However, it should be noted that with an anisotropic tensor, it is possible to have nonzero values of \mathbf{K} and \mathbf{K}' in the boundary subcells. In this case, the boundary conditions can be satisfied by using the anisotropy to orient the tensors so that they mix in a direction tangent to the boundary. That is, $\hat{\mathbf{b}}_3 \cdot \mathbf{K}_3 = 0$ and $\hat{\mathbf{b}}_3 \cdot \mathbf{A}_3 = 0$, where $\hat{\mathbf{b}}_3$ is a unit vector normal to the boundary. In the discrete operator, the boundary conditions can be satisfied by separately orienting \mathbf{K} (and \mathbf{K}') along isopycnal contours, $\mathbf{K} \cdot \mathbf{L} = 0$, in subcells adjacent to a bottom boundary, and setting $\mathbf{b} \cdot \mathbf{K} = 0$ in subcells adjacent to a lateral boundary, where \mathbf{b} is the horizontal component of $\hat{\mathbf{b}}_3$.

c. Tapering of the diffusion tensor

The diffusion tensor \mathbf{K} is tapered according to the prescription of Large et al. (1997, their appendix B), by two tapering functions that range in value from 0 to 1. The first applies when the isopycnal slopes are too steep and falls off rapidly to 0 as the maximum slope approaches 0.3 (note: the original value of the maximum slope was 0.01). The second tapering function applies in the upper ocean and reduces the diffusivity at points at which the distance to the surface along isopycnal surfaces is less than a prescribed Rossby radius. Both of these tapering functions are applied in the 0.2° runs. In the 0.1° runs, the second tapering function was replaced with a function that reduces the diffusivity only at points above the boundary-layer depth diagnosed from the KPP vertical mixing scheme. It falls off linearly from 1 to 0 between H_B and $0.9H_B$, where H_B is the KPP boundary layer depth. Computation of the first tapering function is relatively expensive, and so, rather than evaluating it in every subcell, a single tapering function is computed for the four upper subcells in each full cell and another for the four lower subcells. The root-mean-square slope in the four subcells is used to evaluate the tapering functions.

As discussed in sections 3a and 3b, horizontal diffusion was added in the upper ocean in the 0.2° branch runs AI1' and AA2' and in the 0.1° branch run A'. This

can be trivially implemented by simply not tapering the upper-left elements of the diffusion tensor \mathbf{K}_3 in (10). This is equivalent to adding an additional horizontal diffusion

$$\nabla \cdot (1 - f_1 f_2) \mathbf{K} \cdot \nabla \phi, \quad (\text{A5})$$

where f_1 and f_2 are the tapering functions.

REFERENCES

- Barnier, B., L. Siefridt, and P. Marchesio, 1995: Thermal forcing for a global ocean circulation model using a three-year climatology of ECMWF analyses. *J. Mar. Syst.*, **6**, 363–380.
- Bartello, P., and G. Holloway, 1991: Passive scalar transport in β -plane turbulence. *J. Fluid Mech.*, **223**, 521–536.
- Böning, C. W., F. O. Bryan, W. R. Holland, and R. Döscher, 1996: Deep-water formation and meridional overturning in a high-resolution model of the North Atlantic. *J. Phys. Oceanogr.*, **26**, 1142–1164.
- Cuny, J., P. B. Rhines, P. P. Niiler, and S. Bacon, 2002: Labrador Sea boundary currents and the fate of the Irminger Sea Water. *J. Phys. Oceanogr.*, **32**, 627–647.
- Danabasoglu, G., and J. C. McWilliams, 1995: Sensitivity of the global ocean circulation to parameterizations of mesoscale tracer transports. *J. Climate*, **8**, 2967–2987.
- Dukowicz, J. K., and R. D. Smith, 1997: Stochastic theory of compressible turbulent fluid transport. *Phys. Fluids*, **9**, 3523–3529.
- Figueroa, H. A., and D. B. Olson, 1994: Eddy resolution versus eddy diffusion in a double gyre GCM. Part I: The Lagrangian and Eulerian description. *J. Phys. Oceanogr.*, **24**, 387–401.
- Gent, P. R., and J. C. McWilliams, 1990: Isopycnal mixing in ocean circulation models. *J. Phys. Oceanogr.*, **20**, 150–155.
- , J. Willebrand, T. J. McDougall, and J. C. McWilliams, 1995: Parameterizing eddy-induced tracer transports in ocean circulation models. *J. Phys. Oceanogr.*, **25**, 463–474.
- Griffies, S. M., 1998: The Gent–McWilliams skew flux. *J. Phys. Oceanogr.*, **28**, 831–841.
- , 2004: *Fundamentals of Ocean Climate Models*. Princeton University Press, 496 pp.
- , A. Gnanadesikan, R. C. Pacanowski, V. D. Larichev, J. K. Dukowicz, and R. D. Smith, 1998: Isonutral diffusion in a z -coordinate ocean model. *J. Phys. Oceanogr.*, **28**, 805–830.
- , R. C. Pacanowski, and R. W. Hallberg, 2000: Spurious diapycnal mixing associated with advection in a z -coordinate ocean model. *Mon. Wea. Rev.*, **128**, 538–564.
- Haidvogel, D. B., and T. Keffer, 1984: Tracer dispersal by mid-ocean mesoscale eddies. *Dyn. Atmos. Oceans*, **8**, 1–40.
- Hall, M. M., and H. L. Bryden, 1982: Direct estimates and mechanisms of ocean heat transport. *Deep-Sea Res.*, **29**, 339–359.
- Hirst, A. C., and T. J. McDougall, 1996: Deep-water properties and surface buoyancy flux as simulated by a z -coordinate model including eddy-induced advection. *J. Phys. Oceanogr.*, **26**, 1320–1343.
- Holloway, G., and S. Kristmannsson, 1984: Stirring and transport of tracer fields by geostrophic turbulence. *J. Fluid Mech.*, **141**, 27–50.
- Käse, R. H., and W. Krauss, 1996: The Gulf Stream, the North Atlantic Current, and the origin of the Azores Current. *The Warmwater sphere of the North Atlantic Ocean*, W. Krauss, Ed., Gebrüder-Borntrager, 291–337.
- Killworth, P. D., 1997: On the parameterization of eddy transfer, Part I: Theory. *J. Mar. Res.*, **55**, 1171–1197.
- Large, W. G., J. C. McWilliams, and S. C. Doney, 1994: Oceanic vertical mixing: A review and a model with a nonlocal boundary layer parameterization. *Rev. Geophys.*, **32**, 363–403.
- , G. Danabasoglu, S. C. Doney, and J. C. McWilliams, 1997: Sensitivity to surface forcing and boundary layer mixing in the NCAR CSM ocean model: Annual-mean climatology. *J. Phys. Oceanogr.*, **27**, 2418–2447.
- , —, J. C. McWilliams, P. R. Gent, and F. O. Bryan, 2001: Equatorial circulation of a global ocean climate model with anisotropic horizontal viscosity. *J. Phys. Oceanogr.*, **31**, 518–536.
- Lavender, K. L., R. E. Davis, and W. B. Owens, 2002: Observations of open-ocean deep convection in the Labrador Sea from subsurface floats. *J. Phys. Oceanogr.*, **32**, 511–526.
- Levitus, S., 1982: *Climatological Atlas of the World Ocean*. NOAA Prof. Paper, 13, 173 pp. and 17 microfiche.
- McDougall, T. J., 1987: Neutral surfaces. *J. Phys. Oceanogr.*, **17**, 1950–1967.
- , and P. C. McIntosh, 2001: The temporal-residual-mean velocity. Part II: Isopycnal interpretation and the tracer and momentum equations. *J. Phys. Oceanogr.*, **31**, 1222–1246.
- Pacanowski, R. C., and S. G. H. Philander, 1981: Parameterization of vertical mixing in numerical models of the tropical oceans. *J. Phys. Oceanogr.*, **11**, 1443–1451.
- Pickart, R. S., D. J. Torres, and R. A. Clarke, 2002: Hydrography of the Labrador Sea during active convection. *J. Phys. Oceanogr.*, **32**, 428–457.
- Roberts, M., and D. Marshall, 1998: Do we require adiabatic dissipation schemes in eddy-resolving ocean models? *J. Phys. Oceanogr.*, **28**, 2050–2063.
- Semtner, A. J., and Y. H. Mintz, 1977: Numerical simulation of the Gulf Stream and mid-ocean eddies. *J. Phys. Oceanogr.*, **7**, 208–230.
- Smith, R. D., 1999: The primitive equations in the stochastic theory of adiabatic stratified turbulence. *J. Phys. Oceanogr.*, **29**, 1865–1880.
- , and P. R. Gent, Eds., 2002: Reference manual for the Parallel Ocean Program (POP): Ocean component of the Community Climate System Model (CCSM2.0 and 3.0). [Available online at <http://www.cesm.ucar.edu/models/ccsm2.0/pop/>.]
- , and J. C. McWilliams, 2003: Anisotropic horizontal viscosity for ocean models. *Ocean Modell.*, **5**, 129–156.
- , J. K. Dukowicz, and R. C. Malone, 1992: Parallel ocean general circulation modeling. *Physica D*, **60**, 30–61.
- , M. E. Maltrud, F. O. Bryan, and M. W. Hecht, 2000: Numerical simulation of the North Atlantic Ocean at $1/10^\circ$. *J. Phys. Oceanogr.*, **30**, 1532–1561.
- Treguier, A. M., I. M. Held, and V. D. Larichev, 1997: Parameterization of quasi-geostrophic eddies in primitive equation ocean models. *J. Phys. Oceanogr.*, **27**, 567–580.
- Veronis, G., 1975: The role of ocean models in tracer studies. *Numerical Models of Ocean Circulation*, National Academy of Science, 133–146.
- Visbeck, M., J. Marshall, T. Haine, and M. Spall, 1997: Specification of eddy transfer coefficients in coarse-resolution ocean circulation models. *J. Phys. Oceanogr.*, **27**, 381–402.
- Watts, D. R., K. L. Tracey, J. M. Bane, and T. J. Shay, 1995: Gulf Stream path and thermocline structure near 74°W and 68°W . *J. Geophys. Res.*, **100**, 18 291–18 312.